Derivation of component aerosol direct radiative forcing at the top of atmosphere for clear-sky oceans

Tom X.-P. Zhao[a,b,*], Hongbin Yu[c,d], Istvan Laszlo[b],
Mian Chin[c], William C. Conant[e]

[a]*Coorporate Institute of Climate Study, Earth System Science Interdisciplinary Center, UMCP, College Park, MD 20742, USA*
[b]*Center of Satellite Applications and Research, NOAA/NESDIS, Camp Springs, MD 20746, USA*
[c]*Laboratory for Atmospheres, NASA/GSFC, Greenbelt, MD 20771, USA*
[d]*Goddard Earth Science and Technology Center, UMBC, Baltimore, MD 21250, USA*
[e]*Department of Atmospheric Sciences, University of Arizona, Tucson, AZ 85721, USA*

Abstract

A two-step approach is proposed to derive component aerosol direct radiative forcing (ADRF) at the top of atmosphere (TOA) over global oceans from 60°S to 60°N for clear-sky condition by combining Terra CERES/MODIS-SSF shortwave (SW) flux and aerosol optical thickness (AOT) observations with the fractions of component AOTs from the GSFC/GOCART model. The derived global annual mean component ADRF is $+0.08 \pm 0.17 \, \text{W/m}^2$ for black carbon, $-0.52 \pm 0.24 \, \text{W/m}^2$ for organic carbon, $-1.10 \pm 0.42 \, \text{W/m}^2$ for sulfate, $-0.99 \pm 0.37 \, \text{W/m}^2$ for dust, $-2.44 \pm 0.84 \, \text{W/m}^2$ for sea salt, and $-4.98 \pm 1.67 \, \text{W/m}^2$ for total aerosols. The total ADRF has also been partitioned into anthropogenic and natural components with a value of -1.25 ± 0.43 and $-3.73 \pm 1.27 \, \text{W/m}^2$, respectively. The major sources of error in the estimates have also been discussed. The analysis adds an alternative technique to narrow the large difference between current model-based and observation-based global estimates of component ADRF by combining the satellite measurement with the model simulation.
© 2007 Elsevier Ltd. All rights reserved.

Keywords: Aerosol direct radiative forcing; Aerosol optical thickness

1. Introduction

Since aerosols cause the largest uncertainties in assessing the climate forcing of atmospheric constituents associated with anthropogenic activity [1], various approaches have been used to study global aerosol radiative forcing and to narrow the related uncertainties. In this paper, we refer the term "aerosol radiative forcing" in a rather broad way, which is the effect of both natural and anthropogenic aerosols on the radiative fluxes. The aerosol radiative forcing due to aerosol effect on radiative fluxes through the scattering and absorption of

aerosol particles is referred as aerosol direct radiative forcing (ADRF). Traditionally, model calculations were used to compute the global ADRF [2–10]. Since the publication of the third assessment report of the Intergovernmental Panel on Climate Change (IPCC) in 2001, satellite measurements have been more and more widely used in the study of global ADRF [11–23]. However, there are still large differences between observation-based and model-based global estimates of ADRF. A comprehensive review of recent model- and measurement- based studies of ADRF has been given by Schulz et al. [10] and Yu et al. [24], respectively.

Due to successful launch of more advanced satellite instruments, such as the Moderate Resolution Imaging Spectroradiometer (MODIS), more aerosol information contents become available from satellite measurement, which makes it possible for an in-depth study of global ADRF using satellite observations. For example, MODIS aerosol size information (such as fine-mode aerosol fraction of aerosol optical thickness (AOT)) has been utilized to discriminate ensemble anthropogenic aerosol from natural aerosol (NA) [25] and to estimate the global ADRF of anthropogenic aerosols [18–19,21,25,26]. However, it is still difficult to use satellite observations alone to further discriminate aerosols into more detailed components (such as sea salt (SS), dust (DU), sulfate (SU), black carbon (BC), and organic carbon (OC)) over the globe as well as to derive their direct radiative forcing. Since the ADRF of different aerosol components are different (e.g., even the sign of a forcing can be reversed), the accurate estimation of component ADRF becomes important and deserves to be explored. Here, we present an approach that combines satellite derived ADRF from the Clouds and Earth's Radiant Energy System (CERES) instrument on the EOS-Terra satellite with the optical thickness fractions of major aerosol components from the Goddard Chemistry Aerosol Radiation and Transport (GOCART) model to determine the ADRF for the major aerosol components over the global oceans from 60°S to 60°N. The satellite observation and model simulation are introduced in Section 2; the methodology is explained in Section 3; evaluation on the approach is performed in Section 4; results are given in Section 5; uncertainty estimations and some discussions are presented, respectively, in Sections 6 and 7; and a summary is given in the closing section.

2. Satellite and model products

In this study, aerosols are divided into five major components: BC, OC, SU, DU, and SS, following the aerosol classification in the GOCART model [27–30]. The total AOT (or τ) is the sum of the component AOTs (or $\tau_{TOT} = \tau_{BC} + \tau_{OC} + \tau_{SU} + \tau_{DU} + \tau_{SS} = \sum_{i=1}^{5} \tau_i$). Moreover, BC, OC, and SU are further grouped as anthropogenic aerosols (AN) after removing the contributions from natural OC (OCn) and natural sulfate (SUn) (or $\tau_{AN} = \tau_{BC} + \tau_{OC} + \tau_{SU} - \tau_{OCn} - \tau_{SUn}$). τ_{OCn} and τ_{SUn} are calculated in the GOCART model and can be output for our application. The NAs are determined by subtracting the anthropogenic component from the total aerosols ($\tau_{NA} = \tau_{TOT} - \tau_{AN}$). τ_{TOT}, τ_{BC}, τ_{OC}, τ_{SU}, τ_{DU}, τ_{SS}, τ_{AN}, and τ_{NA} from the GOCART model are used to determine the fraction (r_i) of individual component AOT for BC, OC, SU, DU, SS, AN, and NA using the relationship $r_i = \tau_i / \tau_{TOT}$ ($i =$ BC, OC, SU, DU, SS, AN, and NA). The aerosol optical parameter used to derive ADRF in our approach is the AOT at 0.55 μm (or $\tau_{0.55}$) from the Terra/CERES-MODIS single scanner footprint (SSF) Edition-1A data.

The Terra/CERES-MODIS SSF shortwave (SW) fluxes at the top of atmosphere (TOA) and the standard MODIS AOTs aggregated to the CERES footprints are used in the current study. The Terra CERES SSF product [31,32] combines CERES radiances and fluxes with scene information from coincident high spectral and spatial resolution MODIS measurements, and assimilated meteorological fields. Radiative fluxes are determined using angular distribution models (ADMs) described in Loeb et al. [33]. There are two aerosol products in the SSF data, called AVHRR-type and MODIS product, respectively. Detailed description, comparison, and validation of these two aerosol products can be found in Zhao et al. [34,35]. The MODIS product is selected and used here due to its better global and regional validation result against the surface AERONET observations. The SSF MODIS aerosol product is obtained by averaging the standard 10 km MODIS aerosol products [36,37] over the ocean in each CERES footprint weighted by the CERES point spread function (PSF). The MODIS Collection 3 aerosol product (MOD04) was used in the Edition-1A SSF data. SSF AOTs at $\lambda = 0.55$ μm and TOA SW fluxes of 2001 are used in our analysis since the two SSF aerosol products for the same year had been analyzed and evaluated in detail [34,35]. The SSF-MODIS AOTs are averaged to obtain daily and monthly mean values. The daily and monthly AOTs (τ_{TOT}) are then partitioned

into major aerosol components (τ_i, $i =$ BC, OC, SU, DU, SS, AN, NA) by using the component fractions (r_i) from the GOCART model with $\tau_i = r_i$ (GOCART) $\times \tau_{TOT}$ (SSF-MODIS).

The GOCART model [29] is driven by the assimilated meteorological fields from the Goddard Earth Observing System Data Assimilation System (GEOS DAS) so that its results are more suitable for a comparison with actual observations than a global aerosol model driven by a general circulation model (GCM) output. The model results have been extensively compared with observations from field programs, ground-based network, and satellite remote sensing [27–30,38,39]. The comparison of monthly averaged model results with the AERONET measurements has shown that the model reproduces the seasonal variations at most of the AERONET sites [29,40], which is critical to our current study focused on the study of seasonal ADRF. According to Chin et al. [39], the GOCART AOTs over ocean compare well statistically with those from MODIS and AERONET. Comparisons of multiple aerosol models with MODIS and other satellite observations in the AeroCom framework also show that GOCART falls in the model group that has a better agreement with the MODIS satellite observations [41].

In the current study, our focus is on the examination of global seasonal and annual mean distributions of component ADRF. The analysis is confined to the ocean areas between 60°S and 60°N due to the relatively poor quality of satellite-derived aerosols at high latitudes caused by weak sunlight and high surface reflectance of snow and ice [24].

3. Methodology

A two-step approach is developed to derive the TOA component ADRF. The first step is to derive TOA total ADRF. The instantaneous TOA ADRF for a given time (t) and given location at latitude (θ) and longitude (φ) is defined as

$$\Delta F(t, \theta, \varphi) = F^0(t, \theta, \varphi) - F^a(t, \theta, \varphi), \tag{1}$$

where F^0 and F^a are TOA upward SW fluxes in the absence and presence of aerosols, respectively.

Since F^0 for a given region and time depends only on solar zenith angle (SZA), a simple regression procedure described in Loeb and Kato [13] is used for deriving F^0. Specifically, instantaneous SSF TOA fluxes are plotted against the SSF AOTs at 0.55 μm in 1° SZA increments. The regression for each 1° SZA interval is extrapolated to zero AOT and the corresponding solar flux is used for the "no aerosol" flux (see Fig. 1 for SZA = 15.5° bin and $F^0 = 78.08$ W/m^2). A six-order polynomial fit is applied to the "no aerosol" fluxes for all of the 1° SZAs. The F^0 value for a given area is then determined by averaging the fluxes retrieved from the polynomial fit. The SSF footprints used for deriving F^0 are selected by using the SSF clear strong index (CSI) with a criterion of CSI $\geqslant 99\%$ (see Appendix A for a detailed description of CSI) to avoid sub-pixel residual cloud contamination discussed in Zhao et al. [34,35].

It was found in the study of ADRF [19,20,23] that mapped MODIS τ (0.55 μm) in the CERES cloud-free footprints is smaller than the standard MODIS τ (0.55 μm) and that the derived ADRF is biased towards CERES cloud-free ocean skies, especially when ΔF is derived from very clear SSF footprints (such as CSI $\geqslant 99\%$). This is mainly due to the difference between CERES SSF cloud screening and the standard MODIS aerosol cloud screening. The difference is further amplified in mapping the clear sub-pixels to the big CERES footprints. To correct this bias, Zhang et al. [19] introduced a correction factor to their final ADRF based on the difference of CERES/MODIS SSF clear-sky τ (0.55 μm) and the standard MODIS τ (0.55 μm). Loeb and Manalo [20] avoided this bias by using the mapped MODIS radiances and standard MODIS τ (0.55 μm) to derive the clear-sky SW fluxes directly from a narrow band approach rather than using the SSF SW fluxes based on the CERES broadband approach and the averaged MODIS τ (0.55 μm) for the CERES cloud-free footprints. Here, we adopted a different procedure. It was found in our validation of the SSF aerosol optical properties [34,35] that CERES/MODIS-SSF AOT and Ångström Exponent (AE or α) compare better to that of the AERONET for the SSF footprints selected with a threshold of CSI in the range of 85–90% rather than 99%. Consistent checks performed over broad open oceans [34,35] for the footprints with CSI > 85% and CSI > 99% also support the conclusion from the AERONET validation. Based on these results, we use the threshold CSI $\geqslant 85\%$ rather than CSI $\geqslant 99\%$ to select the CERES footprints used for deriving F^a to avoid the bias towards the cloud-free ocean skies in the calculation of ΔF with Eq. (1).
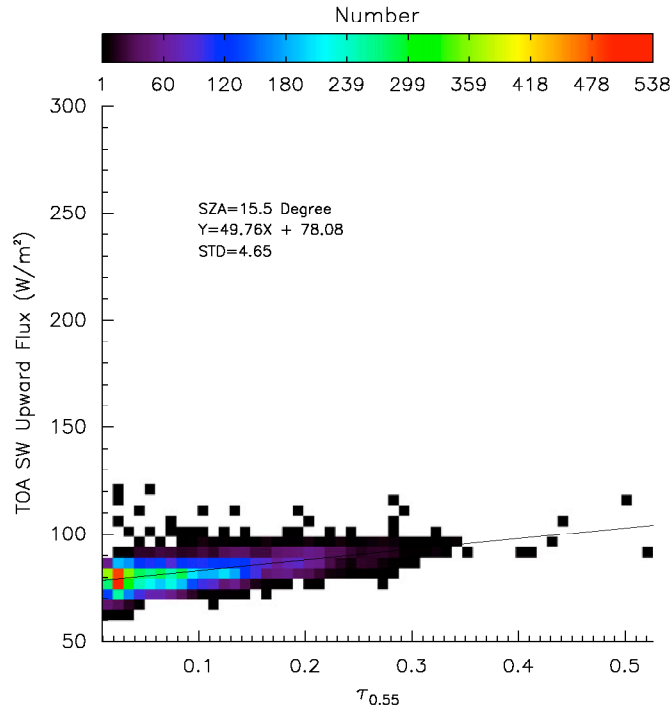
Fig. 1. Scatter plot of TOA SSF SW upward flux versus SSF-MODIS aerosol optical thickness at 0.55 μm for all the SSF footprints with CSI ⩾ 99% and solar zenith angles (SZA) in the bin of 15.0° ⩽ SZA ⩽ 16.0°. The linear regression line and formula are also displayed.

After the instantaneous TOA ADRF, $\Delta F(t, \theta, \varphi)$, is determined from Eq. (1), it needs to be converted to a daily mean, $\Delta F(d, \theta, \varphi)$. Zhang et al. [19] calculated scaling factors to convert the instantaneous CERES/SSF ADRF to a daily average for Terra overpass by using a four-stream radiative transfer model for every hour and 12 aerosol models over four latitude belts centered at 15°N, 15°S, 45°N, 45°S in different seasons. The scaling factors are clustered around 2.0 (have a mean of 2.0 and a standard deviation of 0.1) so that this mean value (2.0) was used by Zhang et al. [19] to convert Terra instantaneous ADRF to diurnally averaged ADRF. The diurnally averaged ADRF is different from the instantaneous ADRF derived during satellite overpass time due to two main factors: the variation of SZA and aerosol optical properties during a day. Since Terra satellite AOT retrieved during a specific overpass time could represent the daily averaged AOT with a 2% error on the annual average [42], the scaling factors should mainly depend on the changes in SZA during a day. For a given location, we also use this factor 2.0 to convert $\Delta F(t, \theta, \varphi)$ to $\Delta F(d, \theta, \varphi)$ for Terra SSF data. The value of $\Delta F(d, \theta, \varphi)$ is further averaged to obtain the seasonal and annual means, which are the focus of this study. Actually, the uncertainty associated with the scaling procedure in the determination of $\Delta F(d, \theta, \varphi)$ is further smoothed by seasonal and annual averaging. The uncertainty introduced in the ADRF by using a single scaling factor is about 0.25 W/m^2, as discussed later in Section 6.1.

The second step is to estimate ADRF for individual aerosol components (including BC, OC, SU, DU, SS, AN, and NA). According to Boucher et al. [43], Boucher and Tanré [11], and Bellouin et al. [16], the direct radiative forcing of non-absorbing or weakly absorbing aerosols is, to a good approximation, proportional to $(e^{-\tau}-1)$ for τ at 0.55 μm. Based on this empirical relationship, we first average $\Delta F(d, \theta, \varphi)$ and τ into a $1° \times 1°$ grid, then partition grid $\Delta F(d, \theta, \varphi)$ into a natural component ΔF_{NA} according to

$$\Delta F_i(d, \theta, \varphi) = \Delta F(d, \theta, \varphi) \times (e^{-\tau_i} - 1)/(e^{-\tau} - 1), \qquad (2)$$

due to the weak absorbing properties of the NAs. Here $i = $ NA or other non- or weakly-absorbing aerosols. This relationship implicitly assumes that the aerosol radiative efficiency (RE), defined as the radiative forcing at the top of the atmosphere per unit AOT [25], of component i is equal to that of total aerosols. As shown later in the uncertainty discussion of Section 6.2, the uncertainty introduced due to this assumption is

$\delta_{NA} \approx 0.09$ W/m^2 for the natural component. To avoid a relatively large error caused by the assumption in Eq. (2) for absorbing anthropogenic aerosols, we derive the anthropogenic component $\Delta F_{AN}(d, \theta, \varphi)$ by subtracting the natural component from the total forcing, i.e. $\Delta F_{AN}(d, \theta, \varphi) = \Delta F(d, \theta, \varphi) - \Delta F_{NA}(d, \theta, \varphi)$, rather than applying Eq. (2) directly. We estimate that the uncertainty in the forcing of the anthropogenic component is close to that of the natural component ($\delta_{AN} - \delta_{NA} = 0.09$ W/m^2).

Similarly, the total forcing ΔF can be further partitioned into a SS component ΔF_{SS} and a DU component ΔF_{DU}. ΔF can also be partitioned into a sulfate component ΔF_{SU} and an OC component ΔF_{OC} since they are either non-absorbing or weakly absorbing in the visible wavelengths. Detailed discussions on the related uncertainties for these aerosol components will be discussed in Section 6.2. Due to the strong absorbing nature of BC, which is mostly anthropogenic, the partitioning approach of Eq. (2) is not proper anymore to derive its direct forcing. Instead, we determine ΔF_{BC} by subtracting ΔF_{SU}, ΔF_{DU}, ΔF_{SS}, and ΔF_{OC} from the total forcing ΔF, which is similar to deriving the anthropogenic component, ΔF_{AN}, by subtracting the natural component from the total forcing. The daily forcing values for the individual components and total aerosols are averaged to obtain monthly, seasonal, and annual mean values. The seasonal and annual mean results will be reported in Section 5 of this paper.

4. Comparison and evaluation

4.1. General comparison

In Fig. 2, the annual mean TOA ADRF (Fig. 2a) derived from the first step of our approach for the SSF data of 2001 is compared with the calculation [17] from the Fu-Liou broadband radiation model (Fig. 2b) using the merged standard MODIS and GOCART aerosol optical properties as the radiation model input [44]. The general patterns in their global distribution compare reasonably well, such as relatively strong negative ADRF in the east coast of China, the Bay of Bengal, and the Arabian Sea; minor negative ADRF over the southern tropical oceans; strong negative ADRF in the west coast of central-south Africa and over the middle latitude oceans of both hemispheres. These general patterns are consistent with those of global AOT distribution, which is shown in Fig. 2c.

Detailed comparison is further performed over 13 selected regions (see Fig. 3) over the global oceans. The results are summarized in Table 1 along with the global mean value. The averaged values obtained from seven other observation-based estimates [24] are also listed for a comparison. The difference between the SSF ADRF values and the means of other observation-based estimates are comparable in most of the regions to the difference between the model calculated values and the means of other observation-based estimates. These differences are much smaller than the spatial standard deviation (ε) of SSF or model ADRF. Both SSF and model ADRF values over the 13 regions and the global oceans are somewhat less than the means of other observation-based estimates. However, these differences can be considered small compared to the magnitude of spatial standard deviation of SSF and model ADRF over the same regions, as well as considering different aerosol types prevailing over the regions as shown below.

We also plot the regional and global annual mean ADRF for the major aerosol components and their corresponding AOT over the ocean in Fig. 4. In regions 1, 2, 4, 5, 6, 8, 9, 10, 11, 12, 13, and 14 (global ocean), the ADRF of natural component is larger (more negative) than that of anthropogenic component, especially for Regions 6, 9, and 13, due to the relatively strong influence of DU over Region 6 and SS over Regions 9 and 13. It is also interesting to note that, in Region 4, sulfate ADRF is the highest, followed, respectively, by that of SS, DU, OC, and BC, which is consistent with the heavy influence of industrial pollutions over the east coast of China. In Region 3, the ADRF of anthropogenic component is dominant due to the industrial pollutions from Europe. Sulfate component accounts for most of the anthropogenic contribution to the ADRF, while DU particles account for most of the natural contribution. These features of component ADRF in Region 3 are consistent with the prevailing aerosol types (industrial pollution from Europe and DU particles from Africa). In Region 7, the ADRF values of natural and anthropogenic components are comparable due to the influence of both DU particles and industrial pollutions originated from the African continent and the Indian subcontinent, respectively.
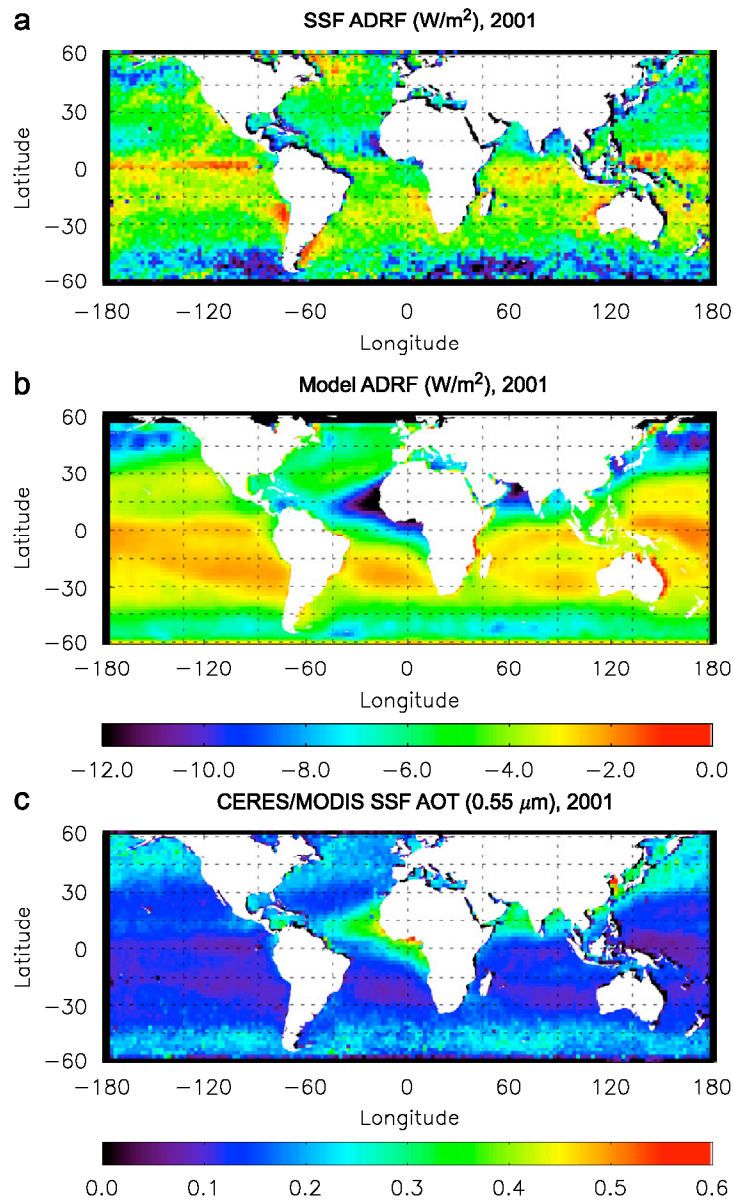
Fig. 2. Global distribution of annual mean TOA ADRF calculated from (a) the CERES/SSF satellite data in our analysis and (b) the Fu–Liou radiation model in Yu et al. [24]. (c) The corresponding annual mean SSF-MODIS aerosol optical thickness at 0.55 μm used in our analysis.

4.2. Comparison with the field experiments

Three intensive field experiments on aerosol and radiation observations are compared with our calculations for a further evaluation on our approach. These field experiments are selected because they were performed either in the same year of 2001 of our study or in several years near 2001 and the compiled observations represent an averaged scenario.

The first case is the Indian Ocean Experiment (INDOEX) [45,46] performed over the tropical Indian Ocean (25°S–25°N; 40°E–100°E) during the northern hemisphere dry (winter) monsoon season in 1996, 1998, and 1999. The INDOEX provides the most complete compilation of observational data that can link the aerosol
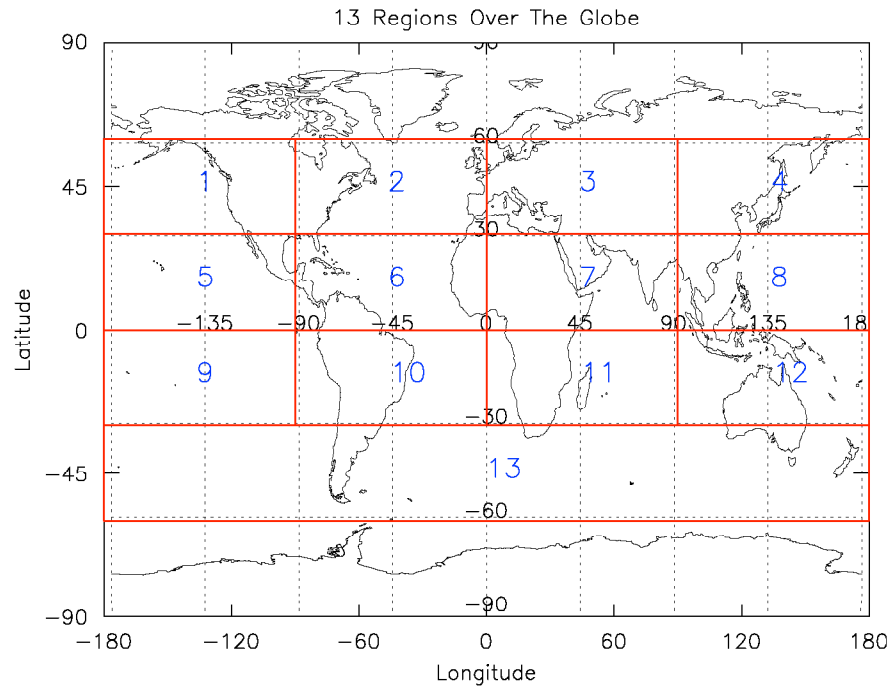
13 Regions Over The Globe

Fig. 3. Thirteen regions over the global oceans in which the annual mean TOA ADRF calculated from the CERES/SSF satellite data in our analysis and from the Fu-Liou radiative transfer model in Yu et al. [24] are compared. These 13 regions are similar to that used in Yu et al. [24].

Table 1
Comparison of annual mean TOA ADRF (or ΔF) derived from recent observation-based calculations, our analysis, and the Fu-Liou radiation model calculation over the global oceans and in oceanic portion of 13 regions (refer to Fig. 3)

Number of regions	Other observations[a]		SSF		Difference ΔF_S–ΔF_O	Model		Difference ΔF_M–ΔF_O
	ΔF_O (W/m²)	STD	ΔF_S (W/m²)	ε		ΔF_M (W/m²)	ε	
1	−6.8	0.16	−5.0	1.7	1.8	−6.3	2.9	0.5
2	−6.5	0.16	−4.4	1.5	2.1	−5.6	2.1	0.9
3	−8.0	0.22	−8.5	8.8	−0.5	−4.2	3.6	3.8
4	−9.7	0.18	−5.7	3.4	4.0	−8.4	3.2	1.3
5	−4.4	0.19	−4.2	1.4	0.2	−4.2	1.1	0.2
6	−7.9	0.20	−5.7	2.5	2.2	−7.6	3.1	0.3
7	−9.3	0.24	−6.3	3.5	3.0	−5.7	4.4	3.6
8	−4.9	0.15	−4.8	2.2	0.1	−4.5	1.9	0.4
9	−3.5	0.21	−3.5	0.7	0.0	−3.0	0.3	0.5
10	−4.6	0.21	−3.9	2.1	0.7	−3.6	1.9	1.0
11	−4.7	0.16	−3.7	1.5	1.0	−3.7	1.8	1.0
12	−4.3	0.19	−3.7	3.1	0.6	−3.2	1.1	1.1
13	−5.6	0.16	−5.5	2.1	0.1	−5.6	1.7	0.0
14[b]	−5.4	0.18	−5.0	2.8	0.4	−4.5	3.1	0.9

[a]The other observations or ΔF_O are taken from Yu et al. [24] and were obtained by averaging the values of seven estimates and STD is the standard deviation of the seven estimates. The ΔF_S (or ΔF_M) is the mean value of all the grid points in the individual regions and ε is the corresponding spatial standard deviations.
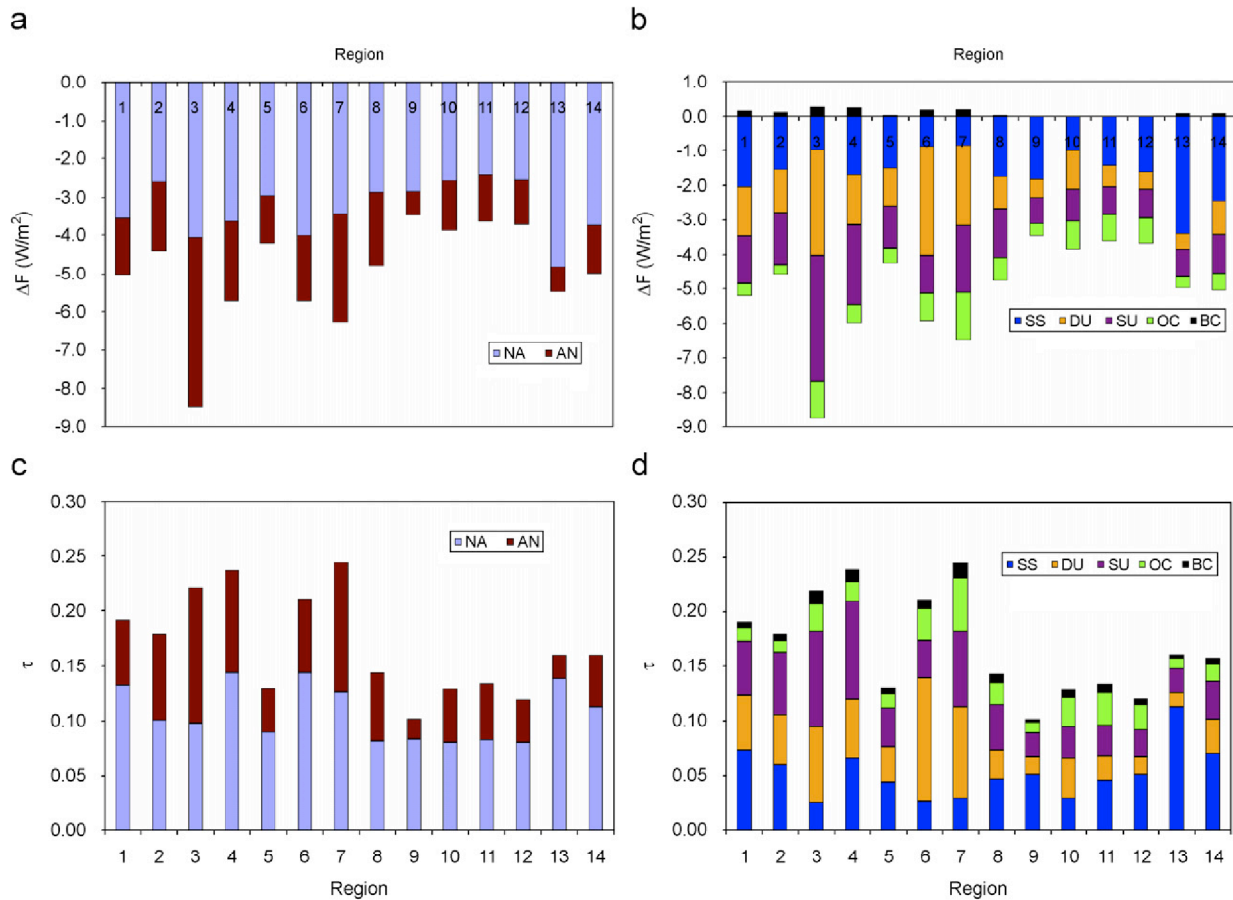[b]Region 14 represents the global oceans.

Fig. 4. Column diagrams of (a, b) annual mean component ADRF and (c, d) the corresponding AOT in the 13 oceanic regions defined in Fig. 3 and over the global ocean (named region 14).

forcing with the chemical and microphysical compositions over the region and can be used to verify our partitioning calculation. The northern part of the region (5°N–25°N; 40°E–100°E) is heavily influenced by industrial pollutions from the Indian subcontinent due to a dominant off-shore wind pattern during the winter monsoon season. The averaged AOT is about 0.2 and about $80 \pm 10\%$ is due to the anthropogenic sources [46], which agrees within the standard deviation to our 0.21 averaged AOT and $70 \pm 15\%$ anthropogenic contribution over the same region (5°N–25°N; 40°E–100°E) in the winter season. The INDOEX compiled component AOTs from various observations are 38% (SU, including ammonia), 12% (DU), 11% (SS), 11% (BC), 24% (organics plus fly ash), 2% (potassium), and 2% (residual unknown components) with the standard error of $\pm 15\%$ [46]. These values agree very well with our component AOT fractions for the winter season, which are $39 \pm 6\%$ (SU), $14 \pm 10\%$ (DU), $8 \pm 6\%$ (SS), $9 \pm 2\%$ (BC), and $30 \pm 9\%$ (OC).

Rajeev and Ramanathan [47] (see their Fig. 7) calculated the ADRF for the northern hemisphere Indian Ocean (NHIO) and the time period of January–March of 1998 and 1999 by using AVHRR AOT and CERES/VIRS-SSF SW fluxes. The values of TOA ADRF are $-5.3 \, \mathrm{W/m^2}$ (1998) and $-7.0 \, \mathrm{W/m^2}$ (1999) and the corresponding averaged AOTs at 0.63 μm are 0.178 and 0.235, respectively. Our value of ADRF for the same region in the winter season is $-5.5 \, \mathrm{W/m^2}$ and the corresponding AOT value is 0.198 at 0.55 μm. Fig. 5 displays the regional maps of AOT and ADRF from our calculation for the NHIO. It is seen that aerosol loading reaches the maximum in the coast of the Indian subcontinent over both the Arabian Sea sector and the Bay of Bengal sector and the corresponding ADRF can be up to $-10 \, \mathrm{W/m^2}$. Very similar distributions were also obtained by Rajeev and Ramanathan [47] (see their Plates 4 and 5).

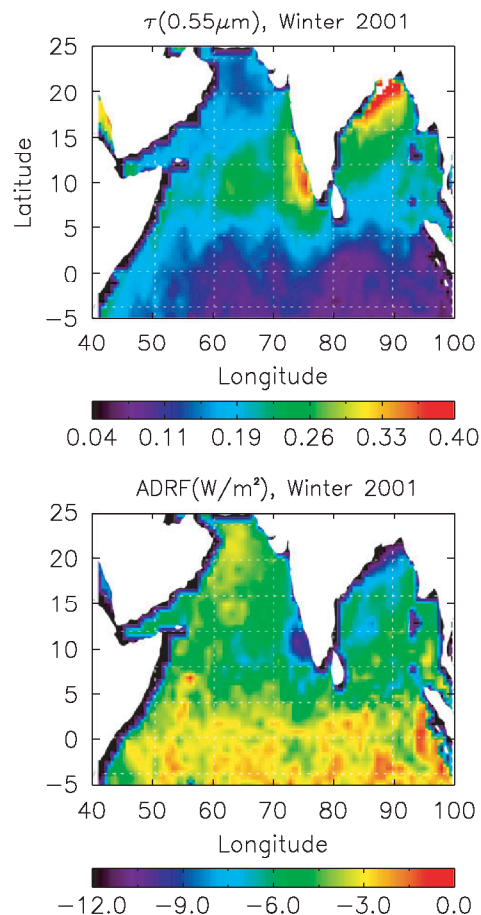Fig. 5. (a) Map of winter seasonal mean of τ at $0.55\,\mu m$ and (b) the corresponding TOA ADRF from our calculation for the northern hemisphere Indian Ocean (NHIO).

Based on a multiple-scattering Monte Carlo radiation model resulted from the compilation of the microphysical, chemical, optical, and lidar data during the INDOEX, Podgorny and Ramanathan [48] (see their Fig. 8) calculated the ADRF for three components (soot, DU, and the remaining species) for a typical scenario ($\tau = 0.4$) over the NHIO. The ADRF obtained by their model calculation for the clear-sky case is about $+0.67\,W/m^2$ (soot), $-0.95\,W/m^2$ (DU), and $-8.67\,W/m^2$ (the remaining species). Our values in the areas with AOT $\geqslant 0.35$ (a mean value of 0.398) in Fig. 5a are $+0.11\pm0.23\,W/m^2$ (BC), $-1.00\pm0.54\,W/m^2$ (DU), and $-10.46\pm3.23\,W/m^2$ (the remaining species). Our values for the DU and remaining species agree well with the radiation model calculation from Podgorny and Ramanathan [48] but our value for BC is much lower, which is mainly due to the uncertainty of partitioning for strong absorbing aerosols in our approach and will be discussed in more detail in Section 6.2.

The latitude variations of winter seasonal mean AOT and ADRF for the major aerosol components are shown in Fig. 6 by averaging over longitude ranges 50–100°E. The AOT of the anthropogenic component is dominant near the coast with SU contributing the most, followed by the contributions of OC and BC. NA is a minor component near the coast, especially SS, and increases gradually towards the open oceans. The anthropogenic AOT decreases rapidly near the northern side of the Intertropical Convergence Zone (ITCZ) and becomes eventually lower than the natural AOT near the southern side of the ITCZ. The contribution of SS to the natural AOT gradually increases toward the open oceans and surpasses the contribution of DU at about 12°N. Correspondingly, the ADRF of anthropogenic component is dominant near the coast (with SU contributing the most) and decreases rapidly toward the open oceans. However, the ADRF of NAs gradually
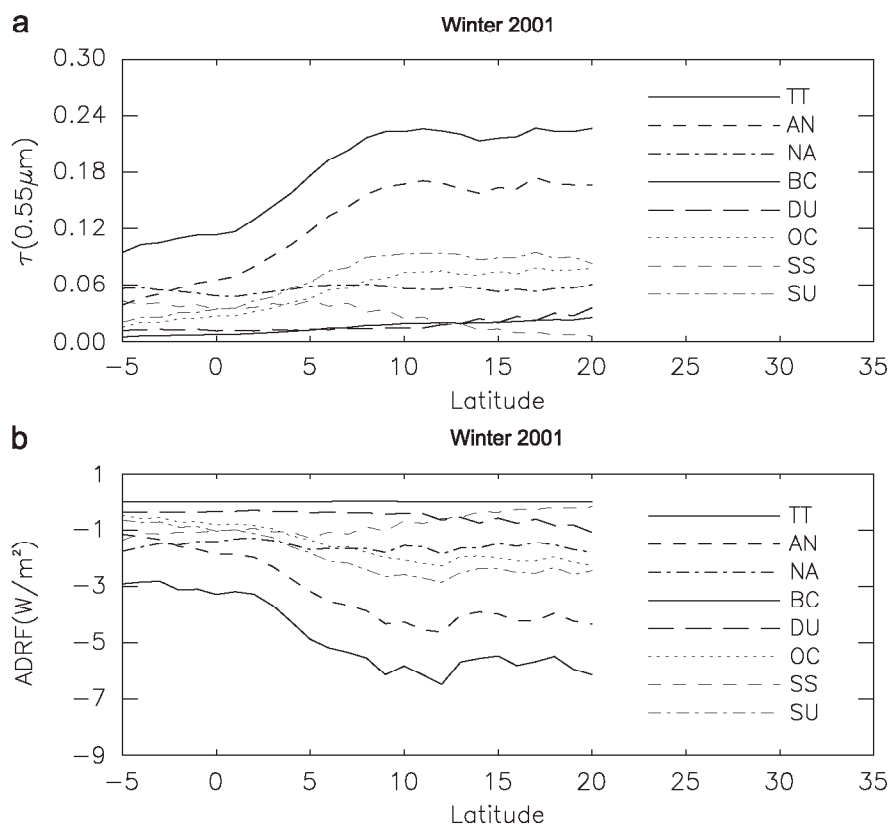
Fig. 6. (a) The latitudinal distribution of winter seasonal mean of component AOT at 0.55 μm and (b) the corresponding TOA component ADRF averaged over the longitude ranges 50°–100°E in the INDOEX region.

increases towards the open oceans (especially SS) and becomes dominant eventually near the southern edge of the ITCZ. These reversed latitude variations of anthropogenic and natural aerosols in optical thickness and direct radiative forcing from the coast of the Indian subcontinent to the open ocean had been noticed during the INDOEX field campaigns and are corroborated here by our results with much more details.

The second case is the Asian Pacific Regional Aerosol Characterization Experiment (ACE-Asia) performed in late March through May 2001 over the east Asia and the Northwest Pacific. The goal of the ACE-Asia was to determine and understand the properties and controlling factors of the aerosol in the anthropogenically modified atmosphere of the East Asia and the Northwest Pacific and to assess their relevance for radiative foricing of climate [49]. The compilation of the data from the observations and model calculations for the experiment can be used to verify our partitioning calculation for the ACE-Asia region.

The mean value of AOT observed from the radiometer abroad the NOAA ship *Ronald H. Brown* during a cruise from March 16 to April 20 is 0.43 ± 0.25 at 0.5 μm and the averaged value of TOA ADRF calculated for the cruise is $-10.6\,\text{W/m}^2$ according to Markowicz et al. [50]. An increasing tendency of AOT was observed when the ship traveled from the open Pacific Ocean towards the Asian continent. Based on the ship tracks summarized in Fig. 1 of Markowicz et al. [50], we selected a domain (120°E–150°E; 30°N–40°N) and averaged the SSF AOT and ADRF for the same time period. The value is 0.45 ± 0.18 for AOT and $-9.4 \pm 5.1\,\text{W/m}^2$ for the ADRF, which agree well with the values from the above ship-based measurement and calculation. As shown in Fig. 7, an increasing tendency of AOT from the open Pacific Ocean to the Asia continent is also confirmed in our calculation with more detailed features. For example, natural AOT is dominant over the open ocean and the AOT of the anthropogenic component increases gradually towards the continent and becomes somewhat higher than that of the natural component near the continent.
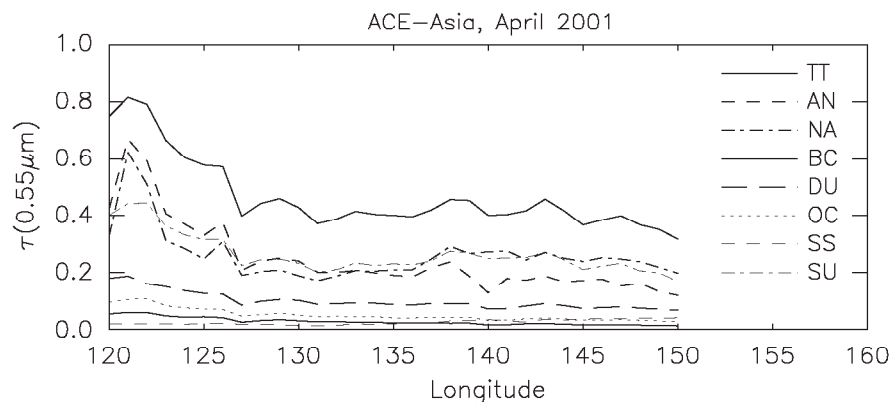
Fig. 7. The longitudinal distribution of component AOT (0.55 μm) averaged for the time period from March 16–April 20, 2001 and over the latitude range 30–40°N in the ACE-Asia region.
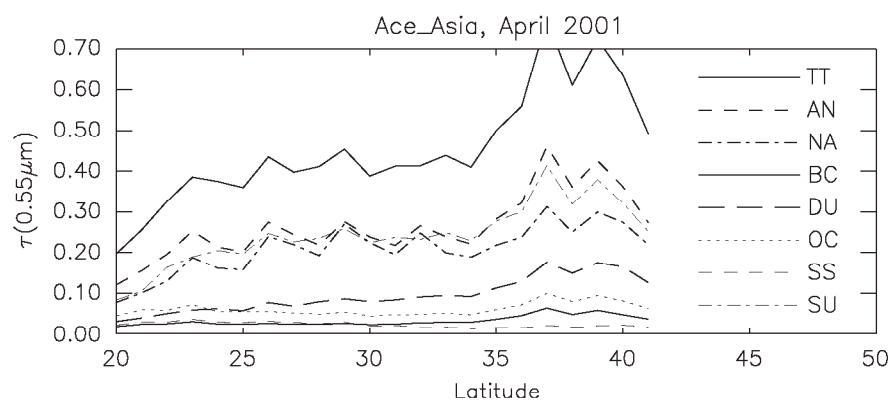

Fig. 8. The latitudinal distribution of component AOT (0.55 μm) averaged for April 2001 and over the longitude range 125.5–130.5°E in the APEX/ACE-Asia region.

A field campaign named Asian Atmospheric Particle Environmental Changes Studies (APEX) was launched in April 2001 over the East China Sea in cooperation with the ACE-Asia experiment. Aerosol radiative forcing in the East China Sea region was studied by combining surface and satellite measurements from the APEX and model simulations [51]. Aerosol radiative forcings were calculated by Nakajima et al. [51] for two surface observation sites, Gosan (33.38°N; 127.17°E) and Amami-Oshima (28.15°N; 129.30°E), and April monthly mean values of AOT (at 0.5 μm) and TOA ADRF are 0.413 ± 0.116, $-10.47 \pm 4.50 \, W/m^2$ at Gosan and 0.390 ± 0.126, $-7.50 \pm 4.49 \, W/m^2$ at Amami-Oshima. For a region of $\pm 3°$ in both latitude and longitude around the two sites, our April monthly mean values of SSF AOT and ADRF are 0.472 ± 0.120, $-8.86 \pm 3.33 \, W/m^2$ at Gosan and 0.373 ± 0.073, $-8.62 \pm 3.65 \, W/m^2$ at Amami-Oshima. Their agreement with the surface observed AOT and calculated ADRF from Nakajima et al. [51] for the two sites is within the standard deviation of SSF AOT and ADRF.

In Fig. 3 of Nakajima et al. [51], they also compared April monthly mean values of the component AOT in a longitude belt between 125.5°E and 130.5°E from 20°N to 42°N for their satellite-retrieved values from the SeaWiFS and the simulations from two three-dimensional aerosol models (CFORS and SPRINTARS). The AOT values from the surface measurement at Gosan and Amami-Oshima sites were also marked in their Fig. 3 for a comparison. Similar to their Fig. 3, we display our AOTs of the component aerosols in Fig. 8. The zonal distribution of our total AOT compares much better with the SeaWiFS retrieval and the two surface measurements than the comparison between the SeaWiFS retrieval and the two model simulations in

Nakajima et al. [51]. The distribution of our DU optical thickness compares better with that from the SeaWiFS retrieval and the SPRINTARS simulation than with the CFORS simulation. Our SS distribution compares well with the two model simulations, but the values from the SeaWiFS retrieval are somewhat higher. For sulfate, our distribution is more close to the two model simulations, especially to the SPRINTARS simulation, and the values from the SeaWiFS retrieval seem to be lower for the region. For the distribution of total carbon (BC + OC), our values are more close to the two model simulations, especially to the SPRINTARS simulation, and the values from the SeaWiFS retrieval are somewhat too high (even higher than the values of sulfate).

A column multiple-scattering Monte Carlo radiation model was developed based on the compilation of the microphysical, chemical, optical, and lidar data during the ACE-Asia [52]. For a region of 100°E–150°E, 20°N–50°N, this model was used to calculate the averaged component AOT and ADRF over the time period 5–15 April 2001 for the mean meteorological and aerosol profiles as predicted by the CFORS model (see Fig. 6 of Conant et al. [52]). The model values averaged over the oceanic area in the domain are compared with the SSF-GOCART component analysis in Fig. 9. Total AOT and component AOTs from the CFORS model are somewhat lower than that from the SSF analysis, especially for SU, DU, and TOT. Actually, similar underestimation of AOT values from the CFORS and SPRINTARS models was observed over the East China Sea during the ACE-Asia period when compared with the SeaWiFS satellite observation and the surface measurement at Gosan and Amami-Oshima sites as mentioned above (see also Fig. 3 of Nakajima et al. [51]). However, the AOT partitioning tendency of the model calculation and the SSF analysis are consistent with SU contributing the most, followed by DU, OC, SS, and BC, respectively. Correspondingly, the ADRF of SU is dominant, followed by DU, OC, SS, and BC, respectively. The difference of individual component ADRF between the Monte Carlo radiation model calculation and the SSF-GOCART component analysis is within the standard deviation of the SSF component ADRF.

The last case is the Chesapeake Lighthouse and Aircraft Measurements for Satellites (CLAMS) field campaign conducted over the Atlantic Ocean off Virginia Beach from 10 July to 2 August 2001 to assess satellite-derived aerosol products and radiative effects [53]. The CERES Ocean Validation Experiment
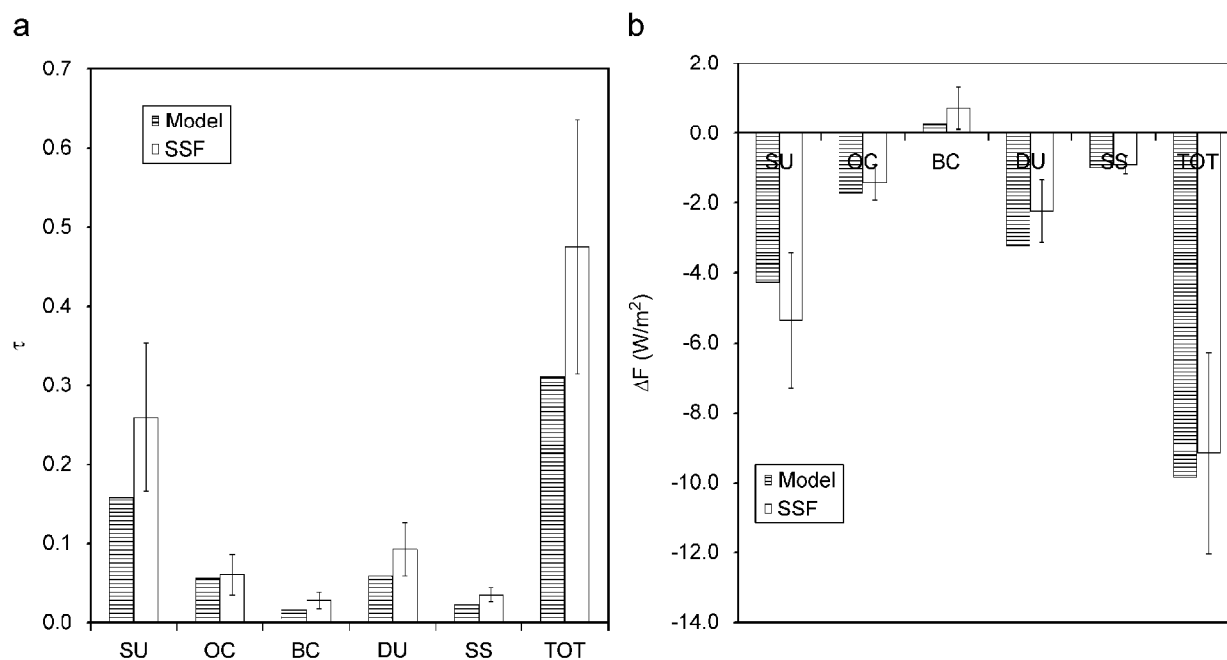

Fig. 9. Partitioning among major aerosol component for (a) AOT and (b) TOA ADRF. Both model-based calculation of Conant et al. [52] and the SSF-GOCART based analysis are presented for a comparison. Data are averaged over the period 5–15 April 2001 during the ACE-Asia Campaign for the oceanic area in the domain of 20–50°N; 100–150°E. ±Spatial standard deviations of the SSF values are displayed with the vertical error bars. The total ADRF of the model is the simple summation of the individual components.
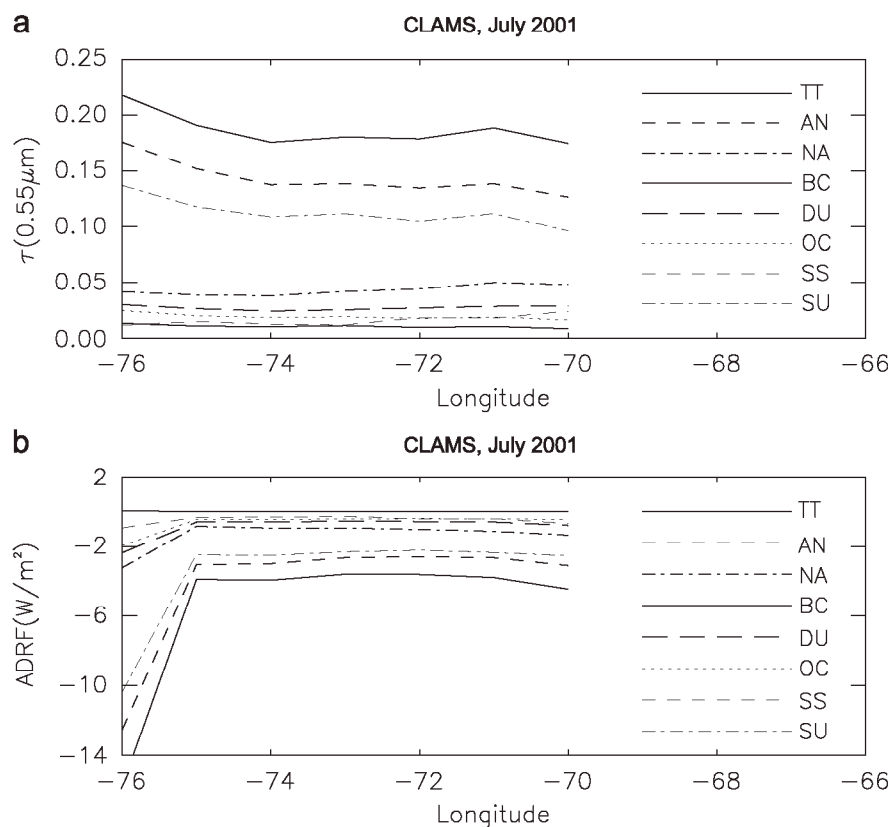
a

b

Fig. 10. (a) The longitudinal distribution of July monthly mean of component AOT at 0.55 μm and (b) the corresponding TOA component ADRF averaged over the latitude range 35–39°N in the CLAMS region.

(COVE) site co-located with the AERONET site at the Chesapeake lighthouse ocean platform is the major surface observational site for the campaign, which is 25 km east of the coast of Virginia at the mouth of the Chesapeake Bay. The July monthly mean value of AOT observed at the COVE AERONET site is 0.227 (0.207 for the fine mode, 0.02 for the coarse mode). The corresponding TOA ADRF, calculated by Zhou et al. [54] using the Fu-Liou broadband radiation model with the proxy data from the COVE site as the model input, is $-9.70\,W/m^2$ ($-8.66\,W/m^2$ for the fine mode and $-1.04\,W/m^2$ for the coarse mode). Since the fine mode aerosols off the Virginia Beach in summer are mainly anthropogenic in origin, the values of find mode and coarse mode can be used to approximate the values of the anthropogenic and natural component, respectively. Our SSF July monthly mean values averaged over the campaign region (35°N–39°N; 74°W–78°W) are 0.203 ± 0.048 for AOT and $-8.40\pm3.49\,W/m^2$ for the TOA ADRF. The corresponding partitioned values for the anthropogenic and natural components are 0.172 ± 0.038 and 0.031 ± 0.01 for AOT and -6.59 ± 2.79 and $-1.81\pm0.72\,W/m^2$ for ADRF. These SSF-GOCART values agree within their standard error with the calculation of Zhou et al. [54].

According to the airborne in situ measurement [55], a major difference between chemical compositions of aerosols observed in the July 2001 CLAMS campaign and in the July 1996 TARFOX campaign for the same region is that sulfate becomes dominant in 2001 while carbonaceous species are dominant in 1996. The dominant contribution from sulfate in the CLAMS campaign is also confirmed in our component aerosol AOT distributions displayed in Fig. 10a. There is also an increasing tendency of AOT from the open ocean towards the coast. This is mainly associated with the enhancement of sulfate aerosols near the coast due to the industrial pollutions transported from the US continent. Correspondingly, the ADRF of total aerosols as well as sulfate component increases rapidly near the coast and the value can be up to $-14\,W/m^2$ for the total aerosol and $-10\,W/m^2$ for the sulfate component (see Fig. 10b).
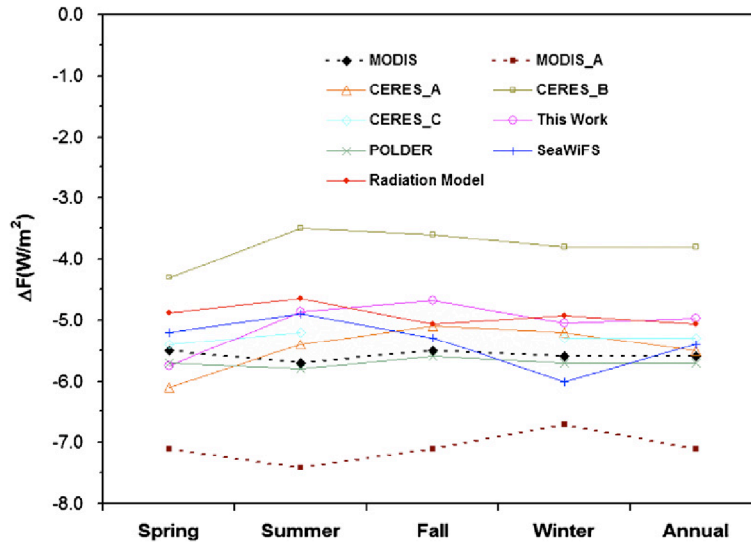
Fig. 11. Global seasonal and annual mean values of TOA ADRF obtained from our analysis and its comparison with some other recent estimates collected in Yu et al. [24].

5. Results

The above comparison and evaluation encourages us to believe that the approach proposed in Section 3 is feasible for the determination of component ADRF over the global oceans. We have applied the approach to the whole year SSF data of 2001, and the results of global seasonal and annual means are presented below.

Fig. 11 displays the global seasonal and annual mean ADRF from our analysis along with the values derived from some other recent works collected in Yu et al. [24]. The global means of total ADRF over ocean in spring (MAM), summer (JJA), fall (SON), winter (DJF), and annual averages from our calculation are -5.8, -4.9, -4.7, -5.1, and -5.0 W/m^2, respectively. The corresponding global mean AOTs are 0.167, 0.158, 0.157, 0.155, and 0.158. The seasonal variation of our result is very close to that of CERES_A since they are based on very similar data. The small magnitude difference (<0.5 W/m^2) is probably due to the difference in data-processing procedures, for example, a narrow band calculation was used in CERES_A [20] but a broadband calculation was performed in the original CERES/SSF data used in our analysis. Our annual mean value (-5.0 W/m^2) agrees well with the observational mean value of -5.5 W/m^2, but is much greater than the model mean value of -3.2 W/m^2 summarized in Yu et al. [20] and in Table 2 of this paper.

The global distributions of annual mean ADRF and the corresponding AOTs for the anthropogenic aerosol component and natural component are displayed in Fig. 12. Relatively strong negative forcing of anthropogenic aerosols is mainly located in the east coast of China and USA, the Bay of Bengal, the Arabian Sea, Europe, the Gulf of Mexico, and the west coast of central–south Africa, which is consistent with the enhanced aerosol loadings due to either bio-mass burning or industrial pollutions over these regions. Major negative ADRF of NAs occurs mainly over the west coast of Africa due to desert DUs and at latitudes higher than 45° in both hemispheres due to SSs. The global and annual mean values of ΔF for individual components are $+0.08$ W/m^2 for BC, -0.52 W/m^2 for OC, and -1.10 W/m^2 for SU, -2.44 W/m^2 for SS, -0.99 W/m^2 for DU, -1.25 W/m^2 for AN, and -3.73 W/m^2 for NA, and the corresponding AOT values are 0.006 for BC, 0.016 for BC, and 0.034 for SU, 0.070 for SS, 0.032 for DU, 0.046 for AN, and 0.112 for NA.

Fig. 13 displays the global seasonal and annual mean ADRF for the component aerosols and their corresponding AOTs. Anti-correlation between the seasonal variations of component ADRF and AOT is observed. For NA, τ_{NA} reaches maximum in spring and minimum in fall, and the corresponding ΔF_{NA} has a negative maximum in spring and a negative minimum in fall. These seasonal features are strongly related to the seasonal variation of SS and DU, which are the two major contributors to NA, with SS contributing the most and DU contributing the second for all seasons (see Fig. 13a). τ_{SS} reaches maximum in winter and

Table 2
Comparison of global and annual mean TOA ADRF for the major aerosol components (AC) over the ocean derived from the CERES/SSF data with recent observation- and model-based estimates

AC	Our estimation		Recent observations[a]	Recent models[b]
	ΔF_i	Uncertainty	ΔF_i	ΔF_i
BC	+0.08	±0.17	–	+0.15 to +0.58
OM	−0.52	±0.24	–	−0.15 to −0.65
SU	−1.10	±0.42	–	−0.21 to −0.96
DU	−0.99	±0.37	–	−0.14 to −1.06[c]
SS	−2.44	±0.84	–	−0.3 to −1.1[c]
AN	−1.25	±0.43	−0.5 to −1.1[d]	−0.60 to −0.64[e]
NA	−3.73	±1.27	−4.7[f]	−1.41[e]
Total	−4.98	±1.67 (33.5%)	−3.8 to −6.5 (−5.5)	−2.3 to −4.7 (−3.2)

[a,b]A range is given for the total ΔF (taken from Yu et al. [24]) with the mean value in a parenthesis. The component values of model-based estimates are compiled from Adams et al. [5], Jacobson et al. [6], Grini et al. [67], Liao et al. [8], Reddy et al. [9], Takemura et al. [7,68], and Schulz et al. [10].

[c]The values for DU and SS from the recent model estimates include the contribution from the longwave radiative forcing.

[d]The observation-based estimates of anthropogenic aerosol forcing are taken from Bellouin et al. [3], Kaufman et al. [25], and Christopher et al. [26] and the uncertainty can be up to ±0.7 W/m².

[e]Values are taken from Reddy et al. [9] and Schulz et al. [10].

[f]The observation-based estimate of natural aerosol forcing is derived by subtracting a median value (−0.8 W/m²) of *AN* forcing (−0.5 W/m² to −1.1 W/m²) from the mean value (−5.5 W/m²) of total aerosol forcing.

minimum in summer (Fig. 13a), which is mainly due to the seasonal variation in the northern hemisphere (NH) since the NH seasonal variation is much stronger than that in the southern hemisphere (SH) (see Fig. 14a). The corresponding ΔF_{SS} reaches negative maximum in winter and negative minimum in summer. On the contrary, τ_{DU} reaches maximum in summer but minimum in winter due to the strong seasonal variation in the NH (see Fig. 14b). The corresponding ΔF_{DU} has a negative maximum in summer and a negative minimum in winter.

τ_{AN} reaches maximum in summer and minimum in winter and the corresponding ΔF_{AN} has a negative maximum in summer and a negative minimum in winter (Fig. 13b). τ_{SU} reaches maximum in spring and minimum in summer due to, respectively, the maximum in the spring of NH and the minimum in the summer of SH (see Fig. 14c), which is consistent with the seasonal variation of ΔF_{SU}, with a negative maximum in spring and a negative minimum in summer (see Fig. 13b). τ_{OC} and τ_{BC} have a peak in both spring and fall (Fig. 13b) due to, respectively, the industrial pollutions in the NH and the biomass burning in the SH (see the example shown in Fig. 14d for OC). This produces different seasonal variations of ΔF_{OC} and ΔF_{BC} in the two hemispheres, but they are consistent with the seasonal variations of τ_{OC} and τ_{BC} in the two hemispheres. The global seasonal variations of ΔF_{OC} and ΔF_{BC} are somewhat smoothed compared to their hemispheric counterparts due to the cancellation effect of the two hemispheric values.

The annual and zonal mean ADRF and AOT for total, natural, and anthropogenic aerosols are displayed in Fig. 15. The features in the ADRF are consistent with those in the AOT. For example, the negative peak of ADRF near 50°S is caused by the SS particles enhanced in the "roaring 40°S band" [34,35] shown in Fig. 16a; Relatively low loading of marine aerosols over the lower latitude oceans of the southern hemisphere produces a relatively small radiative forcing, Africa desert particles over a narrow band centered at about 15°N (see Fig. 16a) are responsible for the sharp enhancement in the negative ADRF from the equator to 15°N in Fig. 15. The high column loading of mixed marine aerosol, DU, and industrial pollution over the northern middle latitudes and high marine aerosol loading at the northern high latitudes, produce a strong ADRF in both northern middle and high latitudes with apparent fluctuations in the northern middle latitudes due to the comparable contributions of several aerosol types from different sources. The negative ADRF of anthropogenic component increases systematically from the SH to the NH (Fig. 15), which is consistent with the systematic increase of anthropogenic aerosol loading from the SH to the NH due to more industrial pollutions in the NH. This is also supported by the strong NH-to-SH gradient of ADRF and AOT for the
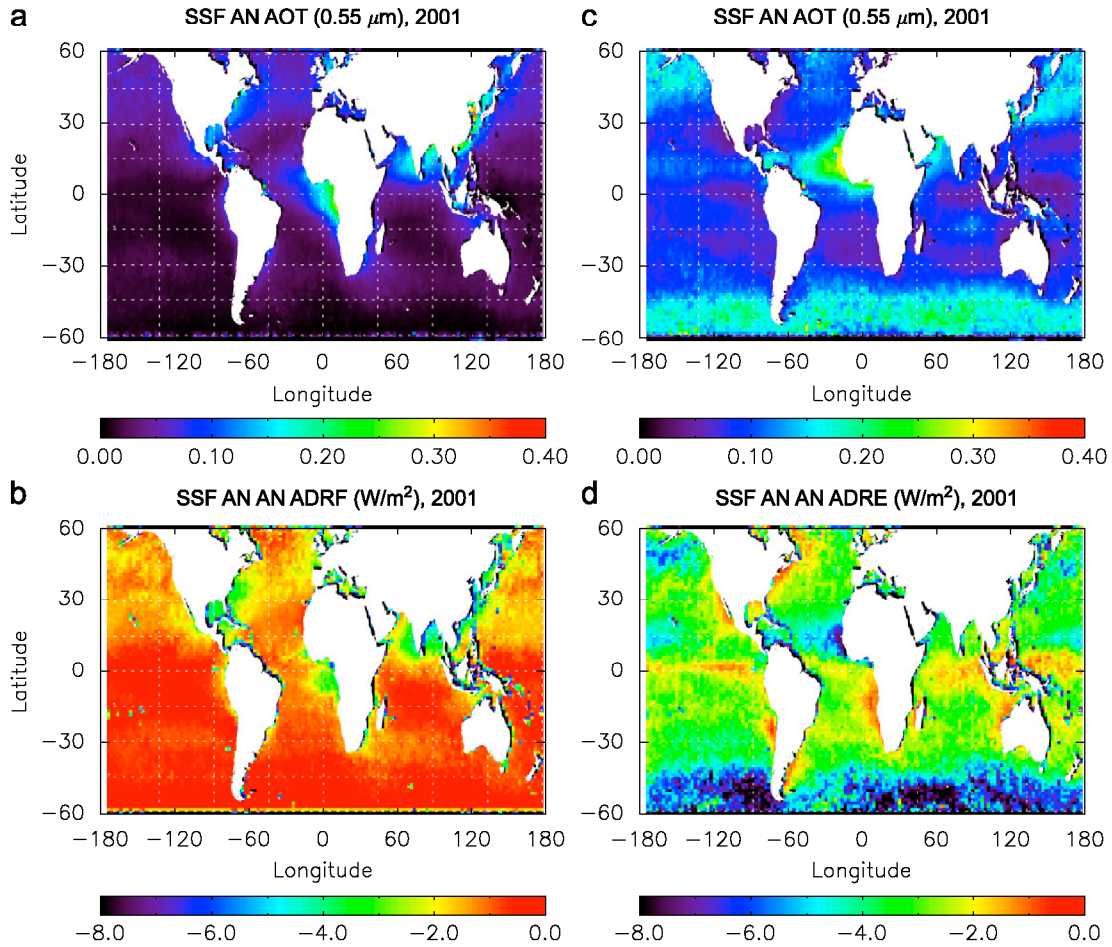
Fig. 12. Global distribution of annual mean AOT at 0.55 μm (top row) and TOA ADRF (bottom row) derived from the CERES/SSF data for the anthropogenic aerosol component (AN) and natural aerosol component (NA).

sulfate component shown in Fig. 16b. The magnitude of ADRF and AOT for OC becomes comparable to that of SU in the tropical regions (see Fig. 16b) due to the contribution of enhanced biomass burning.

6. Uncertainty estimations

6.1. Uncertainties in total ADRF

There are several uncertainties associated with our estimation of TOA total ADRF from the CERES/SSF data. The first error source is associated with the SSF TOA SW clear-sky fluxes, which includes three contributors: uncertainties in calibrated CERES radiances, uncertainties in the conversion of filtered SW radiance to unfiltered SW radiance, and uncertainties in the radiance-to-flux conversion (or ADM model). Wielicki et al. [56] and Priestley et al. [57] estimated that the absolute uncertainty in calibrated CERES SW radiances is about 1%, which corresponds to a 0.4 W/m^2 uncertainty in the averaged clear-sky TOA flux [58]. Loeb et al. [58] also estimated the uncertainties in the conversion of filtered SW radiance to unfiltered SW radiance to be about 1% (or 0.4 W/m^2) in the averaged clear-sky TOA flux over oceans. The uncertainties in the radiance-to-flux conversion in the CERES ADM model would produce an error of 0.2 W/m^2 in clear-sky TOA flux according to the estimation of Loeb et al. [33]. Zhang et al. [18,19] further indicated that not considering aerosol darkening (brightening) over glint (nonglint) regions in an ADM (like CERES ADMs)
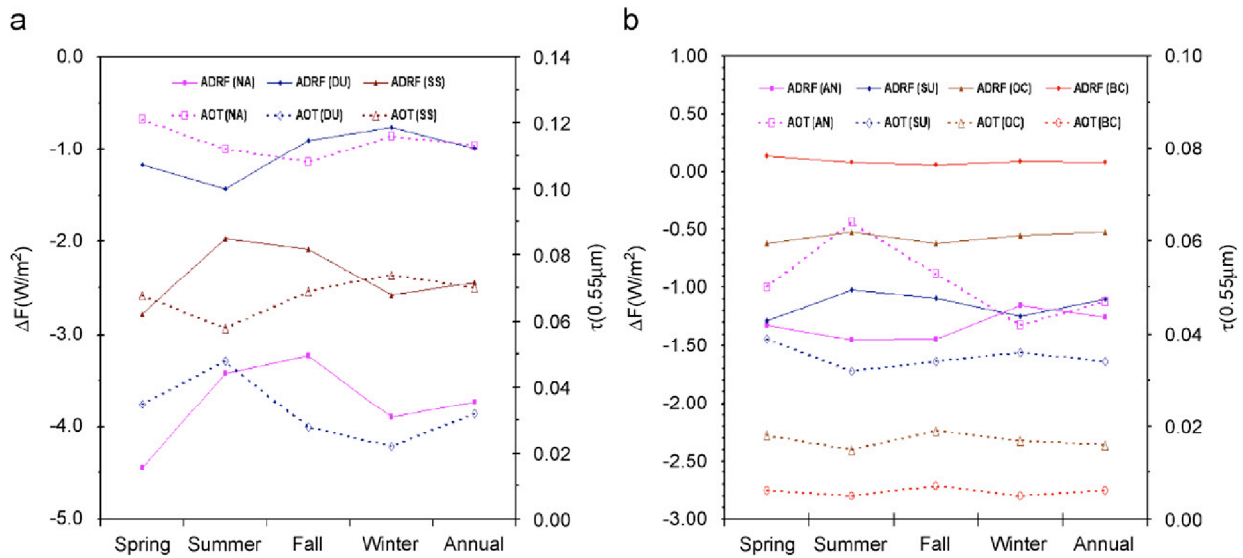
Fig. 13. Global seasonal and annual mean values of AOT at 0.55 μm and TOA ADRF obtained from our analysis for (a) NA, DU, SS and (b) AN, SU, OC, BC.
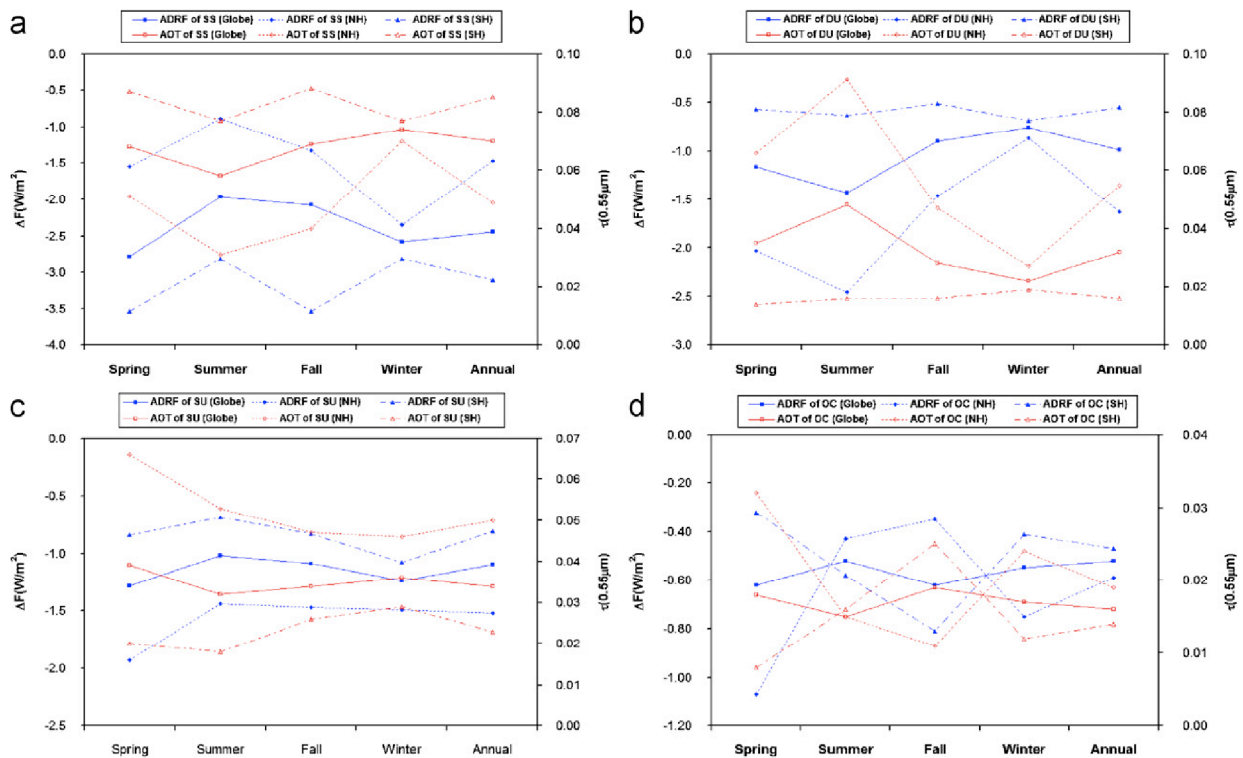
Fig. 14. Global and hemispheric seasonal and annual mean values of AOT at 0.55 μm and TOA ADRF obtained from our analysis for (a) SS, (b) DU, (c) SU, and (d) OC.

may introduce 10% (or 0.64 W/m^2) uncertainties in the instantaneous TOA clear-sky flux, which corresponds to about 0.32 W/m^2 in the averaged TOA clear-sky flux. Assuming these uncertainties are independent to each other, the overall error becomes $(0.4^2 + 0.4^2 + 0.2^2 + 0.32^2)^{1/2} = 0.68$ W/m^2.

Fig. 15. The zonal distribution of annual mean TOA ADRF calculated from the CERES/SSF satellite data over the global ocean and the corresponding annual mean SSF-MODIS aerosol optical thickness at 0.55 μm for total aerosol (TOT), anthropogenic aerosol (AN), and natural aerosol (NA).
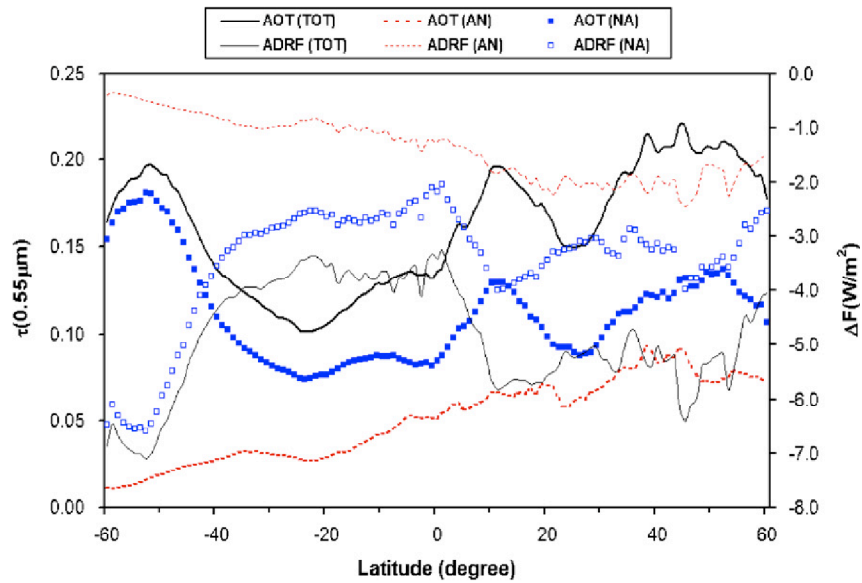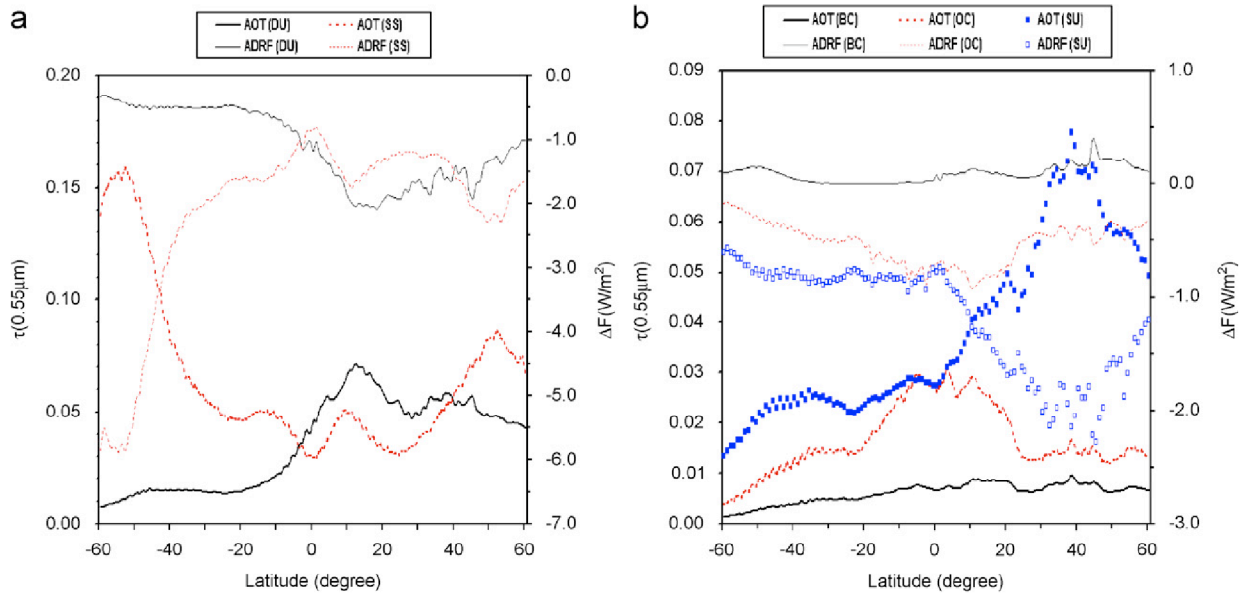

Fig. 16. Similar to Fig. 15, but for (a) DU, SS and (b) BC, OC, SU.

The second error source is the uncertainty associated with the derivation of F^0 discussed in Section 3. An averaged F^0 was determined using the regression relation between τ (0.55 μm) and the TOA ADRF for all the SSF footprints and a regression slop of 41.2 W/m^2 was obtained. According to the approach used in Zhang et al. [19], a 0.03 uncertainty (or the AOT uncertainty of MODIS over the ocean) in τ (0.55 μm) will introduce a $0.03 \times 41.2 = 1.2$ W/m^2 uncertainty in F^0, which agrees well with the estimation of 1 W/m in Loeb and Kato [13].

The third error source is associated with the scaling factor for the conversion of instantaneous ADRF to diurnally averaged value. Since the scaling factor that we used is 2.0 with a standard deviation of 0.1, it is reasonable to consider that the uncertainty of the scaling factor is $0.1/2.0 = 0.05$ (or 5%). It will produce about an uncertainty of 5% in the ADRF, which is about $0.25\,W/m^2$ for the $-4.98\,W/m^2$ global annual mean ADRF.

The last potential error source is sub-pixel cloud contamination due to the relatively coarse spatial resolution (20 km at nadir) of the Terra CERES footprints. To overcome this shortcoming, MODIS high spatial resolution radiances were mapped to a CERES footprint and screened for cloud contamination using the CERES cloud mask scheme at the MODIS pixel level for a given CERES footprint [59]. Specifically, a CSI, which is more conservative for the identification of clear-sky footprints than the traditional clear-sky fraction (see Appendix A), reported for each CERES footprint in the SSF parameters was used to select the clear-sky footprints [34,35]. We only used the SSF footprints with CSI $\geqslant 99\%$ in the determination of F^0 to minimize the uncertainty associated with residual sub-pixel cloud contamination. The optimal 100% threshold was not used in order to obtain a sufficient number of samples over the globe given the relatively coarse spatial resolution of CERES/SSF footprints. To estimate the error introduced in F^0 due to this 1% departure from the optimal 100% threshold, the 99% criterion of CSI was relaxed to 98% and the resultant F^0 is very close to that with CSI $\geqslant 99\%$. Thus, the contamination of residual sub-pixel cloud on our determination of F^0 can be neglected.

The mapped MODIS τ (0.55 μm) into the cloud-free CERES SSF footprints is smaller than the standard MODIS τ (0.55 μm) and results in derived ADRF bias toward CERES cloud-free skies. Since SSF AOT and Angström Exponent compare better to that of the AERONET for the SSF footprints with a CSI threshold in the range of $85\% \leqslant \text{CSI} \leqslant 90\%$ rather than CSI $\geqslant 99\%$ [34,35], we decided to derive F^a using the SSF footprints with CSI $\geqslant 85\%$ rather than with CSI $\geqslant 99\%$ used for the determination of F^0. This will produce a $-1.8\,W/m^2$ difference in instantaneous F^a (or about $-0.9\,W/m^2$ difference in diurnally averaged F^a). As pointed out in Zhao et al. [34,35], cloud effect (including both residual cloud contamination and real enhanced aerosol signal near clouds) will be introduced after the relaxation of CSI threshold from 99% to 85%. It is difficult to quantify exactly how much is due to the contamination and how much is due to the real enhanced aerosol signals. However, the effect of cloud contamination on the ADRF should be less than the combination of the two (or $< -0.9\,W/m^2$).

Assuming that the above four major error sources are not correlated, the overall uncertainty associated with our determination of TOA total ADRF from the SSF data is about $(0.68^2 + 1.2^2 + 0.25^2 + 0.9^2)^{1/2} = 1.67\,W/m^2$ or 34% of the total ADRF.

6.2. Uncertainties in component ADRF

There are two major error sources for the TOA component ADRF. The first is the error inherited from TOA total ADRF discussed above. If we assume the 34% relative uncertainty in the TOA total ADRF is propagated equally into individual components, the values should be 0.027, 0.177, 0.374, 0.337, 0.830, 0.425, and 1.268 (W/m^2) for BC, OM, SU, DU, SS, AN, and NA, respectively.

The second error source associated with the TOA component ADRF is the partitioning uncertainty introduced in Eq. (2) for individual aerosol components. The major assumption of Eq. (2) is that the aerosol radiative efficiency (RE) of non- or weak absorbing aerosols is equal to that of total aerosols. Now, let us check the uncertainties introduced by this assumption for individual aerosol components.

The global mean aerosol RE of our calculation is $-5.0/0.158 = -31.6\,W/m^2/\tau$. DU particles are prevailing in Region 6 of Fig. 3. Therefore, it is reasonable to use the RE value of Region 6 as the DU radiative forcing efficiency, which is $-5.7/0.211 = -27.0\,W/m^2/\tau$. SS is prevailing over Regions 9 and 13 with a RE of $-3.47/0.103 = -33.7\,W/m^2/\tau$ and $-5.48/0.161 = -34.0\,W/m^2/\tau$, respectively. Their AOT weighted RE is $(-33.7 \times 0.103 - 34.0 \times 0.161)/(0.103 + 0.161) = -8.95/0.264 = -33.8\,W/m^2/\tau$, which can be used as the RE of SS particles. The AOT weighted average of DU and SS RE becomes $(-27.0 \times 0.211 - 33.8 \times 0.264)/(0.211 + 0.264) = -14.65/0.475 = -30.8\,W/m^2/\tau$ and can be used as the RE for the NAs.

Thus, the uncertainty introduced by assuming NA RE equals globally averaged RE in Eq. (2) is about $-31.6 - (-30.8) = -0.8\,W/m^2/\tau$ or $-0.8/31.6 = -2.5\%$. The resultant uncertainty in ΔF_{NA} is $\delta_{NA} =$

$0.8\tau_{NA} = 0.8 \times 0.112 = 0.09\,\mathrm{W/m^2}$. The uncertainty in the forcing of the aerosol anthropogenic component should be equal to that of the natural component ($\delta_{AN} \sim \delta_{NA} = 0.09\,\mathrm{W/m^2}$) since ΔF_{AN} is derived using $\Delta F_{AN} = \Delta F - \Delta F_{NA}$ rather than directly using Eq. (2). Similarly, the partitioning uncertainty in the RE of SS and DU introduced by using Eq. (2) is $-31.6-(-33.8) = 2.2\,\mathrm{W/m^2/\tau}$ and $-31.6-(-27.0) = -4.6\,\mathrm{W/m^2/\tau}$, respectively. The corresponding partitioning uncertainty in ΔF_{SS} and ΔF_{DU} can be estimated accordingly and the value is $\delta_{SS} = 2.2\tau_{SS} = 2.2 \times 0.07 = 0.154\,\mathrm{W/m^2}$ and $\delta_{DU} = 4.6\tau_{DU} = 4.6 \times 0.032 = 0.147\,\mathrm{W/m^2}$, respectively.

We have noted in Fig. 4 that sulfate aerosols are dominant over Region 3, especially in winter season due to heavy industrial pollution from the Europe continent. We can use the wintertime RE of aerosols in the region as that of sulfate particles, which is $-2.20/0.059 = -37.3\,\mathrm{W/m^2/\tau}$. The partitioning uncertainty in the RE of SU is $-31.6-(-37.3) = 5.7\,\mathrm{W/m^2/\tau}$. The corresponding partitioning uncertainty in ΔF_{SU} can be estimated as $\delta_{SU} = 5.7\tau_{SU} = 5.7 \times 0.034 = 0.194\,\mathrm{W/m^2}$. Since the left half of Region 11 in Fig. 3 is heavily influenced during summer by biomass burning (or smoke), its RE, $-5.45/0.227 = -24.0\,\mathrm{W/m^2/\tau}$, can be used as the RE of biomass burning smoke. Thus, the partitioning uncertainty in the RE of the smoke is $-31.6-(-24.0) = -7.6\,\mathrm{W/m^2/\tau}$ or $-7.6/31.6 = -24\%$. The corresponding uncertainty in the smoke forcing is $\delta_{SMOKE} = 7.6\tau_{SMOKE} \approx 7.6 \times (\tau_{OC} + \tau_{BC}) = 7.6 \times (0.016 + 0.006) = 0.167\,\mathrm{W/m^2}$. Averaging the smoke forcing efficiency ($-24.0\,\mathrm{W/m^2/\tau}$) and sulfate forcing efficiency ($-37.3\,\mathrm{W/m^2/\tau}$) and the result ($-30.7\,\mathrm{W/m^2/\tau}$) can be considered as the forcing efficiency of anthropogenic aerosols, which agrees well with the value ($-32\,\mathrm{W/m^2/\tau}$) derived by Christopher et al. [26] for anthropogenic aerosols from CERES SSF data using an approach based on MODIS fine aerosol fraction proposed in Kaufman et al. [25]. Since OC (weak-absorbing) and BC (strong-absorbing) are the two major components of biomass burning smoke, The uncertainty of $0.167\,\mathrm{W/m^2}$ for the smoke forcing in our calculation can be considered as the upper (or lower) limit of the uncertainty in ΔF_{OC} (or ΔF_{BC}).

In summary, the uncertainty in component ADRF due to the partitioning is 0.167, 0.167, 0.194, 0.147, 0.154, 0.09, and 0.09$\,\mathrm{W/m^2}$ for BC, OC, SU, DU, SS, AN, and NA, respectively. If we assume they are independent from the uncertainty inherited from the total ADRF (0.027, 0.177, 0.374, 0.337, 0.830, 0.425, and 1.268$\,\mathrm{W/m^2}$ for BC, OC, SU, DU, SS, AN, and NA), the final uncertainties associated with our approach for the determination of component ADRF should be 0.169, 0.243, 0.421, 0.368, 0.844, 0.434, and 1.271$\,\mathrm{W/m^2}$ for BC, OC, SU, DU, SS, AN, and NA, respectively. For ΔF_{BC}, the partitioning uncertainty is dominant compared to the uncertainty inherited from ΔF_{TOT}. The partitioning and the inherited uncertainties are comparable for ΔF_{OC}. For the other aerosol components, the inherited uncertainty in their ADRF is dominant, especially for SS, AN, and NA.

7. Discussion

Observation-based estimation of ADRF mentioned above or in Yu et al. [24] can be further divided into two categories according to how satellite measurements are used. In the first category [17,21–23], satellite measurements of aerosol optical properties are input to a sophisticated radiative transfer model (RTM) for the calculation of radiation fluxes. In the second category [18–20], satellite measurements are used directly to derive ADRF through a correlation analysis of radiation fluxes and AOT, both measured from satellites. Although both are called the observation-based approach, they are fundamentally different.

A radiative transfer model is involved in the first category. Thus, it is critical that consistent aerosol properties should be used both in the AOT retrieval and the radiative transfer calculation as pointed out by Boucher and Tanré [11] and Remer and Kauffman [23]. A natural solution is that aerosol properties used in the AOT retrievals are also used in the radiative transfer calculations, which had been widely adopted by the works in the first category.

Only correlation analysis of retrieved AOT and measured radiation fluxes are involved in the second category (without a direct involvement of radiative transfer models). The accuracy of measured AOTs and radiation fluxes directly impacts the accuracy of ADRF from the correlation analysis. To reduce the error in the final ADRF, AOT or flux measurements should be as accurate as possible. Some procedures can be used to achieve this objective. For examples, Zhang et al. [18,19] introduced aerosol darkening (brightening) over glint (nonglint) regions in their ADM development to better quantify radiance-to-flux conversions. They also multiply a factor to the final ADRF based on the difference of CERES/MODIS SSF clear-sky τ (0.55 μm) and

the standard MODIS τ (0.55 µm) to correct the bias towards cloud-free ocean skies caused by the CERES cloud screening for the SSF footprints. Loeb and Manalo [20] avoided the bias associated with CERES cloud screening by using the mapped MODIS radiances and standard MODIS τ (0.55 µm) to derive the clear-sky SW fluxes directly from a narrow band approach rather than using the SSF SW fluxes based on the CERES broadband approach and the averaged MODIS τ (0.55 µm). We overcome this bias by using the SSF fluxes from those footprints selected from a threshold (CSI $\geqslant$ 85%) based on the validation result of SSF AOT and AE against the AERONET measurement in Zhao et al. [34,35].

CERES SSF data have evolved into different versions. The latest version is Edition 2, in which MODIS Collection 4 aerosol product was used. In the version we used (Edition 1A), MODIS Collection 3 aerosol product was used. The major change of MODIS aerosol product from Collection 3 to the later Collections (such as Collections 4 and 5) is in the aerosol retrievals over land. Since our analyses are limited over the global open oceans, the effect of the changes in the later versions of MODIS aerosol product on our analyses should be minor. In SSF Edition 1A, TOA fluxes are determined using ADMs developed from CERES on TRMM. Edition 2 CERES TOA fluxes are based on ADMs developed from Terra measurements. Thus, the ADM type for inversion classification has changed. The major impact of this change on the CERES TOA SW flux is over high latitude. According to the study of CERES science team (Dr. Norman Loeb, private communication), the difference of monthly mean TOA SW flux between Edition 1 and 2 can be more than 10 W/m^2 for latitude $> 60°$N(S). For 40°N (S) $<$ latitude $<$ 60°N (S), the difference is within 10 W/m^2 with a mean value of about 5.0 W/m^2. For latitude $< 40°$N (S), the difference is generally less than 2.5 W/m^2. Our analysis is limited to latitude $< 60°$N (S), where the difference of the TOA SW fluxes between Edition 1A and Edition 2 is relatively small. This relatively small difference is further removed from the determination of the ADRF in Eq. (1) considering that the difference in the TOA SW fluxes between Edition 1A and Edition 2 is the same for the absence and the presence of aerosols. Thus, we do not expect fundamental changes in our results by using the latest version of the CERES SSF data.

The calculation based on a radiative transfer model with the input of the component aerosol optical properties from global aerosol models is the practical approach used for estimating component ADRF over the globe since satellite technology is still not mature enough to provide component AOTs needed for the determination of global component ADRF. An intensive field campaign for a given location and time period can be used to obtain component aerosol optical properties needed for determining component aerosol radiative forcing in a regional scale through the integration of various measurements. But the global application remains an issue. The approach used in this paper provides an alternative to the widely used radiative transfer model calculation based on the component aerosol optical properties from global aerosol models. It combines CERES satellite measurement with the GOCART model component AOT information without the involvement of radiative transfer models. However, our approach is subject to the influence of the uncertainties of GOCART model simulation.

The development of global aerosol models is now at a stage that simulated global annual mean AOT values are not only in good agreement with each other but also in good agreement with AERONET observations [41]. However, there are still large differences in component AOT simulated by different global aerosol models [41,60], especially for natural components (SS and DU) due to their various emission inventories. Our analysis is not immune from this uncertainty in the component AOTs associated with model simulations, which will be improved gradually with the advancement of global aerosol modeling. Actually, the above comparison of GOCART component AOTs with the observations from the field campaigns justifies its application for the current study.

As a summary, we further compare our component ADRF values with more recent estimates from models and observations in Table 2. Our values for DU and OC agree reasonably well with the recent model estimations. This is probably due to a better simulation of DU and biomass burning in the GOCART model [39], which makes their partitioning more accurate than other components. Our value for BC, $+0.08 \pm 0.17$ W/m^2, is much less than the recent model-based estimates and with a large relative uncertainty, which is associated with our partitioning of BC through a subtraction of two big terms to derive a smaller term. Our calculation for SU is somewhat larger than the recent model-based estimates. This difference is probably due to an externally mixed assumption of aerosols in our partitioning, but sulfate is mainly internally mixed with other compounds over global oceans. Our anthropogenic value agrees reasonably well with the recent

observation-based estimates, but is higher than the model-based estimates. This result corroborates the conclusion of "current model estimates of the anthropogenic ADRF are too weak" in Bellouin et al. [21]. The value of natural ADRF from our analysis is much higher than the current model-based estimates, but agrees reasonably well with the current observation-based estimation. (The difference falls in the range of the uncertainty of our estimation.)

8. Summary

Terra CERES/MODIS-SSF SW flux and AOT at $0.55 \, \mu m$ have been combined with the component AOT fractions from the GOCART model to derive TOA component ADRF over the global cloud-free oceans through a two-step approach. The first step is to drive the total ADRF from the SSF SW fluxes and AOT, and the second step is to partition the total ADRF into the contributions of five major aerosol components by using the AOT fractions of the five component aerosols from the GOCART model simulation. The annual mean values of ADRF averaged over global oceans are $+0.08 \pm 0.17 \, W/m^2$ for BC; $-0.52 \pm 0.24 \, W/m^2$ for OC; $-1.10 \pm 0.42 \, W/m^2$ for SU; $-0.99 \pm 0.37 \, W/m^2$ for DU; $-2.44 \pm 0.84 \, W/m^2$ for SS; $-1.25 \pm 0.43 \, W/m^2$ for AN; $-3.73 \pm 1.27 \, W/m^2$ for NA; and $-4.98 \pm 1.67 \, W/m^2$ for total aerosols.

The error source associated with the SSF TOA SW clear-sky fluxes (including uncertainties in calibrated CERES radiances, uncertainties in the conversion of filtered SW radiance to unfiltered SW radiance, and uncertainties in the radiance-to-flux conversion through the ADM model), the uncertainty introduced in the determination of F^0, the uncertainty associated with the scaling factor of diurnal average, and errors of sub-pixel cloud contamination in the observation of CERES/SSF SW clear-sky fluxes are the four major error sources in the total TOA ADRF calculation. The error from the partitioning is the additional uncertainty to the component ADRF, which is significant for BC. For OC, the partitioning error is comparable to the error inherited from the total ADRF. For the other components, the inherited uncertainty is dominant, especially for SS, AN, and NA. The larger uncertainty in our ADRF for BC is mainly due to the partitioning through a subtraction of two big terms to determine a smaller term. The final uncertainties in the component ADRF might be larger than our current estimates since our analysis is directly influenced by the uncertainty in the GOCART model simulation of major aerosol components associated with the current state of global aerosol modeling. This study focuses only on oceanic regions from 60°S to 60°N since surface disturbance on satellite aerosol retrieval and aerosol forcing calculation over land is not well resolved yet, which is a subject of our future study. To further narrow the uncertainties in the estimation of global component ADRF in the future, an integration of multivariate and multidimensional information from diverse satellite sensors, ground-based instruments, and models is necessary as outlined in Diner et al. [61].

Acknowledgements

Appendix A. Clear Strong Index (CSI)

The CERES cloud mask scheme [62–64] involves a three-step analysis of each re-sampled MODIS pixel. The first step is a simple infrared test that flags pixels that are too cold to correspond to a surface and must be a cloud. The second step involves three kinds of threshold tests comparing pixel radiances to estimated background or clear-sky values for reflectance, infrared brightness temperature, and infrared/near-infrared brightness temperature difference, respectively. The threshold values are specified as functions of geographical location, time, and illumination-observation geometry, based upon empirical analyses, radiative transfer computations, and interpolations. If the three kinds of tests unanimously determine the pixel to be clear, this

pixel is labeled "strong" clear. If one or two tests fail, a series of relaxed tests are performed to determine whether or not the pixel can be labeled as "weak" clear or cloudy. The third step, used for aerosol retrievals only, consists of homogeneity and adjacency tests that are based on the experience of the operational AVHRR aerosol retrieval [65,66]. The tests are used to eliminate residual cloud contamination and cloud shadow effect and are critical for aerosol retrievals. The spatial homogeneity test, which applies to a 2×2 (or 4-km $\times$ 4-km) clear-pixel array, requires that the difference between the maximum and minimum 0.66-μm reflectances in a 2×2 array is less than 0.003. The adjacency test further requires that all eight pixels surrounding the test pixel must be clear.

The CERES cloud mask classifies each CERES sub-pixel (or re-sampled MODIS pixel) as clear, cloudy, bad data, or no retrieval. Each clear pixel is further categorized as "weak" or "strong" to indicate the degree of confidence in the selection (see the above discussions). A CSI is reported for each CERES footprint as one of the CERES parameters which is calculated as the PSF-weighted percent (from 0 to 100) of clear-strong pixels in the CERES field of view (FOV) relative to all the clear and cloudy pixels (bad data and no retrieval pixels are not included in the computation). If there are no clear-strong pixels in the FOV, the coverage is set to zero (CSI $= 0$). If there are clear-strong pixels in the FOV, the coverage is set to 1% or greater ($1 \leqslant CSI \leqslant 100$). It should be noted that the CERES cloud mask often misclassifies cloud-free pixels with heavy dust loadings ($\tau_1 > 2$) as cloudy pixels so that those pixels will rarely accompany a strong clear classification. A more detailed description of the SSF CSI parameter and its definition can be found in Geier et al. [32].

References

[1] IPCC. Climate change 2001: the physical science basis. New York: Cambridge University Press. 870pp.
[2] Hansen J, et al. Climate forcings in the industrial era. Proc Natl Acad Sci 1998;95:12753–8.
[3] Haywood JM, Ramaswamy V, Soden BJ. Tropospheric aerosol climate forcing in clear-sky satellite observations over the oceans. Science 1999;283:1299–303.
[4] Kiehl JT, Schneider TL, Rasch PJ, Barth MC, Wong J. Radiative forcing due to sulfate aerosols from simulations with the National Center for Atmospheric Research Community Climate Model, Version 3. J Geophys Res 2000;105:1441–57.
[5] Adams PJ, Seinfeld JH, Koch DM, Mickley L, Jacob D. General circulation model assessment of direct radiative forcing by the sulfate–nitrate–ammonium–water inorganic aerosol system. J Geophys Res 2001;106:1097–112.
[6] Jacobson MZ. Global direct radiative forcing due to multicomponent anthropogenic and natural aerosols. J Geophys Res 2001;106: 1551–68.
[7] Takemura T, Nakajima T, Dubovik O, Holben BN, Kinne S. Single-scattering albedo and radiative forcing of various aerosol species with a global-three dimensional model. J Climate 2002;15:333–52.
[8] Liao H, Seinfeld JH, Adams PJ, Mickley LJ. Global radiative forcing of coupled tropospheric ozone and aerosols in unified general circulation model. J Geophys Res 2004;109:D16207.
[9] Reddy MS, Boucher O, Balkanski Y, Schulz M. Aerosol optical depths and direct radiative perturbations by species and source type. Geophys Res Lett 2005;32:L12803.
[10] Schulz M, et al. Radiative forcing by aerosols as derived from the AeroCom present-day and pre-industrial simulations. Atmos Chem Phys 2006;6:5095–136.
[11] Boucher O, Tanré D. Estimation of the aerosol perturbation to the Earth's radiative budget over oceans using POLDER satellite aerosol retrievals. Geophys Res Lett 2000;27:1103–6.
[12] Chou MD, Chan PK, Wang M. Aerosol radiative forcing derived from SeaWiFS-retrieved aerosol optical properties. J Atmos Sci 2002;59:748–57.
[13] Loeb NG, Kato S. Top-of-atmosphere direct radiative effect of aerosols over the tropical oceans from the clouds and the Earth's Radiant Energy System (CERES) satellite instrument. J Climate 2002;15:1474–84.
[14] Christopher SA, Zhang J. Shortwave aerosol radiative forcing from MODIS and CERES observations over the oceans. Geophys Res Lett 2002;29:1859.
[15] Sekiguchi M, et al. A study of direct and indirect effects of aerosols using global satellite data sets of aerosol and cloud parameters. J Geophys Res 2003;108:4699.
[16] Bellouin N, Boucher O, Tanre D, Dubovik O. Aerosol absorption over the clear-sky oceans deduced from POLDER-1 and AERONET observations. Geophys Res Lett 2003;30:1748.
[17] Yu H, et al. The direct radiative effect of aerosols as determined from a combination of MODIS retrievals and GOCART simulations. J Geophys Res 2004;109:D03206.
[18] Zhang J, Christopher SA, Remer LA, Kaufman YJ. Shortwave aerosol radiative forcing over cloud-free oceans from Terra: 1. Angular models for aerosols. J Geophys Res 2005;110:D10S23.
[19] Zhang J, Christopher SA, Remer LA, Kaufman YJ. Shortwave aerosol radiative forcing over cloud-free oceans from Terra: 2. Seasonal and global distributions. J Geophys Res 2005;110:D10S24.

[20] Loeb NG, Manalo-Smith N. Top-of-atmosphere direct radiative effect of aerosols over global oceans from merged CERES and MODIS observations. J Climate 2005;18:3506–26.

[21] Bellouin N, Boucher O, Haywood J, Reddy S. Global estimate of aerosol direct radiative forcing from satellite measurements. Nature 2005;438:1138–41.

[22] Chung CE, Ramanathan V, Kim D, Podgorny I. Global anthropogenic aerosol direct forcing derived from satellite and ground-based observations. J Geophys Res 2005;110;D24207.

[23] Remer LA, Kaufman YJ. Aerosol effect on the distribution of solar radiation over the clear-sky global oceans derived from four years of MODIS retrievals. Atmos Chem Phys 2006;6:237–53.

[24] Yu H, et al. A review of measurement-based assessment of aerosol direct radiative effect and forcing. Atmos Chem Phys 2006;6:565–861.

[25] Kaufman YJ, et al. Aerosol anthropogenic component estimated from satellite data. Geophys Res Lett 2005;32:L17804.

[26] Christopher SA, Zhang J, Kaufman Y, Remer LA. Satellite-based assessment of top of atmosphere anthropogenic aerosol radiative forcing over cloud-free oceans. Geophys Res Lett 2006;33:L15816.

[27] Chin M, Rood RB, Lin SJ, Muller JF, Thompson AM. Atmospheric sulfur cycle simulated in the global model GOCART: model description and global properties. J Geophys Res 2000;105:24671–87.

[28] Chin M, et al. Atmospheric sulfur cycle in the global model GOCART: comparison with field observations and regional budgets. J Geophys Res 2000;105:24689–712.

[29] Chin M, et al. Tropospheric aerosol optical thickness from the GOCART model and comparisons with satellite and sun photometer measurements. J Atmos Sci 2002;59:461–83.

[30] Ginoux P, et al. Sources and global distributions of dust aerosols simulated with the GOCART model. J Geophys Res 2001;106: 20255–73.

[31] Wielicki BA, Green RN, Tolson CJ, Fan A. Clouds and the Earth's Radiant Energy System (CERES) algorithm theoretical basis document, overview of cloud retrieval and radiative flux inversion (Subsystem 4.0), Release 2.2, June 2, 1997.

[32] Geier EB, et al. CERES data management system: single satellite footprint TOA/Surface Fluxes and Clouds (SSF) Collection Document. Release 2; Version 1:212pp, Radiation and aerosol branch, Atmospheric Sciences Research, NASA Langley Research Center, Hampton, VA, 2003. Available online at ⟨http://asd-www.larc.nasa.gov/ceres/collect_guide/SSF_CG.pdf⟩.

[33] Loeb NG, et al. Angular distribution models for top-of-atmosphere radiative flux estimation from the Clouds and the Earth's Radiant Energy System instrument on the Tropical Rainfall Measuring Mission satellite. Part I: Methodology. J Appl Meteorol 2003;42:1748–69.

[34] Zhao TX-P, Laszlo I, Minnis L, Remer L. Comparison and analysis of two aerosol retrievals over the ocean in the Terra/CERES-MODIS single scanner footprint (SSF) data: Part I—global evaluation. J Geophys Res 2005;110.

[35] Zhao TX-P, Laszlo I, Minnis P, Remer L. Comparison and analysis of two aerosol retrievals over the ocean in the Terra/CERES-MODIS single scanner footprint (SSF) data: Part II—regional evaluation. J Geophys Res 2005;110.

[36] Tanré D, Kaufman YJ, Herman M, Mattoo S. Remote sensing of aerosol over oceans from EOS-MODIS. J Geophys Res 1997;102: 16971–88.

[37] Remer LA, et al. The MODIS aerosol algorithm, products and validation. J Atmos Sci 2005;62:947–73.

[38] Chin M, et al. A global model forecast for the ACE-Asia field experiment. J Geophys Res 2003;108.

[39] Chin M, et al. Aerosol distribution in the northern hemisphere during ACE-Asia: results from global model, satellite observations, and sunphotometer measurements. J Geophys Res 2004;109.

[40] Liu H, Pinker RT, Holben BN. A global view of aerosols from merged transport models, satellite, and ground observations. J Geophys Res 2005;110:D10S15.

[41] Kinne S, et al. An AeroCom initial assessment—optical properties in aerosol component modules of global models. Atmos Chem Phys 2006;6:1815–34.

[42] Kaufman YJ, et al. Will aerosol measurements from Terra and Aqua polar orbiting satellites represent the daily aerosol abundance and properties. Geophys Res Lett 2000;23:3861–4.

[43] Boucher O, et al. Intercomparison of models representing short-wave radiative forcing by sulfate aerosols. J Geophys Res 1998;103: 16979–98.

[44] Yu H, et al. Annual cycle of global distributions of aerosol optical depth from integration of MODIS retrievals and GOCART model simulations. J Geophys Res 2003;108:D34128.

[45] Satheesh SK, et al. A model for the natural and anthropogenic aerosols over the tropical Indian Ocean derived from Indian Ocean Experiment data. J Geophys Res 1999;104:27421–40.

[46] Ramanathan V, et al. Indian Ocean experiment: an integrated analysis of the climate forcing and effects of the great Indo-Asian haze. J Geophys Res 2001;106:28371–98.

[47] Rajeev K, Ramanathan V. Direct observations of clear-sky aerosol radiative forcing from space during the Indian Ocean Experiment. J Geophys Res 2001;106:17221–35.

[48] Podgorny IA, Ramanathan V. A modeling study of the direct effect of aerosols over the tropical Indian Ocean. J Geophys Res 2001; 106:24097–105.

[49] Huebert BJ, et al. An overview of ACE-Asia: strategies for quantifying the relationships between Asia aerosols and their climatic impacts. J Geophys Res 2003;108:8633.

[50] Markowicz KM, et al. Influence of relative humidity on aerosol radiative forcing: an ACE-Asia experiment perspective. J Geophys Res 2003;108:8662.

[51] Nakajima T, et al. Significance of direct and indirect radiative forcings of aerosols in the East China Sea region. J Geophys Res 2003;108:8658.

[52] Conant BC, et al. A model for the radiative forcing during ACE-Asia derived from CIRPAS Twin Otter and *R/V Ronald H. Brown* data and comparison with observations. J Geophys Res 2003;108:8661.

[53] Smith Jr WL, et al. EOS Terra aerosol and radiative flux validation: an overview of the Chesapeake Lighthouse and Aircraft Measurements for Satellites (CLAMS) experiment. J Atmos Sci 2005;62:903–18.

[54] Zhou M, Yu H, Dickinson RE, Dubovik O, Holben BN. A normalized description of the direct effect of key aerosol types on solar radiation as estimated from Aerosol Robotic Network aerosols and Moderate Resolution Imaging Spectroradiometer albedos. J Geophys Res 2005;110.

[55] Magi BI, et al. Aerosol properties and chemical apportionment of aerosol optical depth at locations off the US East Coast in July and August 2001. J Atmos Sci 2005;62:919–33.

[56] Wielicki BA, et al. Clouds and the Earth's Radiant Energy System (CERES): an earth observing system experiment. Bull Am Meteorol Soc 1996;77:853–68.

[57] Prestley KJ, et al. Post launch radiometric validation of the Clouds and the Earth's Radiant Energy System (CERES) proto-flight model on the Tropical Rainfall Measuring Mission (TRMM) spacecraft through 1999. J Appl Meteorol 2000;39:2249–58.

[58] Loeb NG, et al. Determination of unfiltered radiances from the Clouds and the Earth's Radiant Energy System (CERES) instrument. J Appl Meteorol 2001;40:822–35.

[59] Minnis P, et al. CERES cloud property retrievals from imagers on TRMM, Terra, and Aqua. In: Proceedings of the SPIE 10th international symposium on remote sensing: conference on remote sensing of clouds and the atmosphere. VII: 37–48; Barcelona, Spain, September 8–12, 2003.

[60] Textor C, et al. Analysis and quantification of the diversities of aerosol life cycles within AeroCom. Atmos Chem Phys 2006;6: 5225–46.

[61] Diner DJ, et al. An integrated approach for characterizing aerosol climate impacts and environmental interactions. Bull Am Meteorol Soc 2004;85(10):1491–501.

[62] Trepte Q, et al. Scene identification for the CERES cloud analysis subsystem. In: Proceeding of the AMS 10th Conference on Atmospheric Radiation, Madison, WI, June 28–July 2, 1999, p. 169–172.

[63] Minnis P, et al. CERES cloud properties derived from multispectral VIRS data. In: Proceeding of the EOS/SPIE symposium on remote sensing 1999, vol. 3867, Florence, Italy, September 20–24, 1999, pp. 91–102.

[64] Minnis P, et al. A global cloud database from VIRS and MODIS for CERES. In: Proceeding of the SPIE third International. Asia-Pacific Environmental Remote Sensing Symposium 2002: remote sensing of atmosphere, ocean, environment, and space, vol. 4891, Hangzhou, China, October 23–27, 2002, p. 115–126.

[65] Stowe LL, Davis PA, McClain EP. Scientific basis and initial evaluation of the CLAVR-1 global clear/cloud classification algorithm for the advanced very high resolution radiometer. J Atmos Oceanic Technol 1999;16:656–81.

[66] Vemury S, Stowe LL, Anne VR. AVHRR pixel level Clear-sky classification using dynamic thresholds (CLAVR-3). J Atmos Oceanic Technol 2001;18:169–86.

[67] Grini A, Myhre G, Sundet JK, Isaksen ISA. Modeling the annual cycle of sea salt in the global 3-D model OSLOCTM-Z: concentration, fluxes and radiative impact. J Climate 2002;15:1717–30.

[68] Takemura T, Nozawa T, Emori S, Nakajima TY, Nakajima T. Simulation of climate response to aerosol direct and indirect effects with aerosol transport-radiation model. J Geophys Res 2005;110:D02202.